

1 **Microstructure-based modelling of snow mechanics: experimental** 2 **evaluation on the cone penetration test**

3 Clémence Herny^{1,2}, Pascal Hagenmuller¹, Guillaume Chambon², Isabel Peinke¹, Jacques Rouille¹

4 ¹Univ. Grenoble Alpes, Univ. de Toulouse, Météo-France, CNRS, CNRM, Centre d'Etude de la Neige, Grenoble, France

5 ²Univ. Grenoble Alpes, CNRS, INRAE, IRD, Grenoble INP, IGE, Grenoble, France

6 *Correspondence to:* Clémence Herny (clemence.herny@gmail.com)

7 **Abstract.** Snow is a complex porous material presenting a variety of microstructural patterns. This microstructure largely
8 controls the mechanical properties of snow, although the relation between the micro and macro properties remains to be better
9 understood. Recent developments based on the discrete element method (DEM) and three-dimensional microtomographic data
10 make it possible to reproduce numerically the brittle mechanical behaviour of snow. However, these developments lack
11 experimental evaluation so far. In this study, we evaluate a DEM numerical model by reproducing cone penetration tests on
12 centimetric snow samples. The microstructures of different natural snow samples were captured with X-ray microtomography
13 before and after the cone penetration test, from which the grain displacements induced by the cone could be inferred. The tests
14 were conducted with a modified Snow MicroPenetrometer (5 mm cone diameter), which recorded the force profile at a high
15 resolution. In the numerical model, an elastic brittle cohesive contact law between snow grains was used to represent the
16 cohesive bonds. The initial positions of the grains and their contacts were directly derived from the tomographic images. The
17 numerical model was evaluated by comparing the measured force profiles and the grain displacement fields. Overall, the model
18 satisfactorily reproduced the force profiles in terms of mean macroscopic force (mean relative error of about 20%) and the
19 amplitude of force fluctuations (mean relative error of about 55%), while the correlation length of force fluctuations was more
20 difficult to reproduce (mean relative error of about 40% for two samples out of four and by a factor ≥ 8 for the other two).
21 These characteristics were, as expected, highly dependent on the tested sample microstructure, but they were also sensitive to
22 the choice of the micro-mechanical parameters describing the contact law. A scaling law was proposed between the mechanical
23 parameters, the initial microstructure characteristics and the mean macroscopic force obtained with the DEM numerical model.
24 The model could also reproduce the measured deformation around the cone tip (mean grain displacement relative error of 57%
25 along the horizontal axis), with a smaller sensitivity to the contact law parametrisation in this case. These detailed comparisons
26 between numerical and experimental results give confidence in the reliability of the numerical modelling strategy and opens
27 promising prospects to improve the understanding of snow mechanical behaviour.

28 **1 Introduction**

29 Snow is a brittle and porous material existing on Earth close to its melting point. The thermodynamical conditions in the clouds
30 govern the snowflake morphology and, once deposited on the ground, snow continues to evolve via metamorphism. The snow
31 material is thus characterised by a large variety of microstructural patterns (grain size, grain shape, density) classified into
32 different snow types (Fierz et al., 2009). It has been established that the snow microstructure controls the properties of snow
33 (Shapiro et al., 1997; Johnson and Schneebeli, 1999; Schneebeli, 2004). For instance, weak layers involved in avalanche
34 triggering (Schweizer et al., 2003) are usually constituted of specific snow types (depth hoar, surface hoar, precipitation
35 particle, faceted crystals) characterised by low cohesion and low strength (Jamieson and Johnston, 1992). The link between
36 the snow microstructure and its properties, especially its mechanical properties, is still not well understood, even if it is crucial
37 for many applications, such as avalanche forecasting (Schweizer et al., 2003, Jamieson and Johnston, 1992), snowpack
38 modelling (Calonne et al. 2014), ice core interpretation (Montagnat et al. 2020) or geotechnics (Shapiro et al., 1997). In
39 particular, the brittle failure occurring at high shear rates ($> 10^{-4} \text{ s}^{-1}$) during the release of an avalanche remains represented by
40 very coarse empirical laws (Brun et al., 1992; Bartelt, et al. 2002; Vionnet et al. 2012). In this elastic-brittle regime (rapid and
41 large deformations), the mechanical behaviour of snow is thought to be mainly controlled by bond failures and grain
42 rearrangements (Narita, 1983).

43 The snow microstructure and its evolution can be captured at high resolution (typically 10-50 μm) with X-ray micro
44 tomography imaging (μCT) (Coléou et al., 2001; Freitag et al., 2004; Schneebeli, 2004; Heggli et al., 2011). This non-
45 destructive method preserves the snow microstructure and resolves the shape of snow grains, grain bonds and porosity which
46 is of primary importance for mechanical studies. In particular structural properties of snow, such as density, specific surface
47 area (SSA), correlation length, bond characteristics, can be evaluated from tomographic data (e.g. Schneebeli, 2004;
48 Schneebeli et al., 2004; Hagenmuller et al., 2014a; Calonne et al., 2014; Proksch et al., 2015). The tomographic data are also
49 used as a basis for numerical modelling (Schneebeli, 2004; Schneebeli et al., 2004; Hagenmuller et al., 2015) or
50 calibration/validation data of statistical empirical models retrieving grain-scale physical and mechanical properties from other
51 measurements (e.g. Proksch et al., 2015; Reuter et al., 2019). However, tomographic imaging is time-expensive and not adapted
52 to routine measurements in the field.

53 The mechanical properties of snow are commonly derived from Cone Penetration Test (CPT) measurements, which is an
54 objective and relatively easy-to-set-up method (Schneebeli and Johnson, 1998). This method has been widely used to
55 characterise soil stratigraphy (Lunne et al., 1997) and adapted to snowpack stratigraphy (Gubler, 1975; Schaap and Fohn,
56 1987; Dowd and Brown, 1986; Schneebeli and Johnson, 1998; Mackenzie and Payten, 2002; McCallum, 2014). The CPT
57 provides a force profile by measuring the resisting force exerted on a conic tip penetrating, at a constant rate, into a material.
58 The development of high-resolution digital penetrometers dedicated to snow studies (Schneebeli and Johnson, 1998;
59 Mackenzie and Payten, 2002; McCallum, 2014) has provided the possibility to resolve the force profile at a microscopic scale

60 and capture the high-frequency fluctuations of the force signal up to a metre depth. Such force penetration profiles contain
61 valuable information on the snow structural parameters at macro- and micro-scale (Löwe and van Herwijnen, 2012).
62 Interpretation of the CPT requires a good understanding of the interactions between the cone tip and the snow grains. Several
63 studies aimed to investigate the grain displacement field around the tip. Particle Image Velocimetry (PIV) imaging was
64 performed to quantify the 2D displacement field of snow grains while the tip penetrates into the material (Floyer and Jamieson,
65 2010; Herwijnen, 2013; LeBaron et al., 2014). Peinke et al. (2020) developed a grain tracking algorithm to reconstruct from
66 μ CT the 3D displacement field of snow grains induced by a CPT. All these studies revealed the development of a compaction
67 zone (CZ) in front of the tip.

68 Various mechanical or statistical models have been developed to interpret the CPT penetration signal in terms of mechanical
69 properties. The cavity expansion model (CEM) (Bishop et al., 1945; Yu and Carter, 2002) has been applied to snow by Ruiz
70 et al. (2016) and Peinke et al. (2020). This model considers snow as a continuum and describes the elastic-plastic deformation
71 of the material around the tip in order to retrieve macroscopic material properties (cohesion, friction, etc.). The continuum
72 assumption becomes invalid for a ratio between cone diameter and mean grain diameter lower than 20 typically (Bolton et al.
73 1993), leading to potentially erroneous interpretations of the CPT results. Alternatively, the shot noise model interprets the
74 force signal and its fluctuations as a superposition of independent elastic–brittle ruptures occurring next to the tip (Schneebeli
75 and Johnson, 1999; Marshall and Johnson, 2009; Löwe and van Herwijnen, 2012) and retrieves microstructural properties
76 (bond rupture force, etc.) The penetration process is generally modelled as a Homogeneous Poisson Process (HPP) with a
77 constant intensity (Löwe and van Herwijnen, 2012). Peinke et al. (2019) have generalised the HPP method to account for the
78 transient phase of the penetration process, attributed to the development of the CZ (Peinke et al., 2019). These authors used a
79 Non-Homogeneous Poisson Process (NHPP) considering a depth dependency of the intensity (number of bond failures per
80 penetration increment). Yet, the assumption of independent elastic-brittle rupture events essentially neglects the development
81 of a CZ (Johnson and Schneebeli, 1999; Schneebeli, 2001; Herwijnen, 2013; LeBaron et al., 2014; Ruiz et al. 2017). Therefore,
82 none of these two models appear to fully account for the specificity of snow deformation induced by CPT. Additional
83 investigations are required to better understand the tip interaction with snow and better interpret the force measurements.

84 Recently, numerical approaches have been developed to study the mechanical response of snow by explicitly accounting for
85 the microstructure (Johnson and Hopkins, 2005; Gaume et al., 2015, 2017; Hagenmuller et al., 2015; Wautier et al., 2015;
86 Mede et al. 2018b, 2020; Bobillier et al., 2020, 2021). Snow is described as a granular material and modelled by the discrete
87 element method (DEM) in a high shear rate regime. The complexity of the snow microstructure can be taken into account by
88 feeding the DEM simulations with high-resolution 3D reconstructions obtained with μ CT. These simulations have provided
89 new insights into the snow mechanical behaviour, such as the dependence of snow strength to microstructure properties
90 (Hagenmuller et al., 2015) or the identification of different failure modes in shear loading (Mede et al., 2018b, 2020). The
91 downside of this method is that it is time-consuming, and simulations can only be performed on small samples (up to a few
92 centimetres). Furthermore, these numerical models still lack direct experimental evaluation.

93 In this context, the aim of this study was to evaluate a microstructure-based DEM model using recent CPT experimental data
94 performed in a controlled environment (Peinke et al., 2020). The dataset includes μ CT images of the samples acquired before
95 and after the tests. The deformation induced by the CPT (strain rate of about 10^2 s^{-1} , Reuter et al., 2019) belongs to the elastic-
96 brittle regime (Narita, 1983; Floyer and Jamieson, 2010) and is therefore suitable for DEM simulation. The results of the
97 numerical model are directly compared to experimental data in terms of (1) macroscopic force profile and associated statistical
98 indicators and (2) grain displacements induced by the cone penetration. A systematic sensitivity analysis to DEM mechanical
99 parameters, including Young's modulus, cohesion and friction coefficient, was performed to find the combinations of
100 parameters that best reproduce experimental results. Finally, the role of the microstructure was also investigated by performing
101 DEM simulations for different snow types. The evaluation of the numerical model provides the opportunity to better understand
102 the mechanisms at play during snow deformation in an elastic-brittle regime and better interpret CPT profiles.
103 We first present the experimental dataset and the numerical methods. The data processing used to compare experimental and
104 numerical results is also explained. The results of the DEM, the sensitivity analysis to mechanical parameters and the
105 comparison to experimental results are then presented. The relevance of the DEM model and the limits of our approach are
106 eventually discussed before concluding.

107 **2 Methods**

108 **2.1 Experimental measurements**

109 The experimental dataset used in this study has been acquired by Peinke et al. (2020) and is only briefly presented in this paper.
110 The methodology comprises collection and preparation of snow samples, acquisition of high-resolution micro-tomographic
111 images and cone penetration tests (CPT).

112 **2.1.1 Snow sample preparation**

113 Blocks of natural snow were sampled in the French Alps near Grenoble and stored at -20°C in a cold room. The materials
114 collected were representative of the variety of seasonal snow types (Table 1), namely rounded grains (RG), large rounded
115 grains (RGlr), depth hoar (DH) and precipitation particles (PP), with distinct bulk densities and specific surface areas (SSA).
116 The samples were then prepared in a cold room at -10°C by sieving the different snow types into aluminium cylinders of 20
117 mm height and 20 mm diameter. All samples were prepared at least 24 hours before the measurements in order for the bonds
118 between grains to rebuild after sieving.

119 **2.1.2 Micro-Tomography (μ CT)**

120 Tomographic scans of each sample were acquired before and after performing the CPT to capture the initial and final
121 microstructure of the snow, respectively. An X-ray tomograph (DeskTom130, RX Solutions) operating at a pixel size of $15 \mu\text{m pix}^{-1}$,
122 a voltage of 80 kV and a current of $100 \mu\text{A}$ was used. During tomographic scanning, the samples were maintained

123 at a constant and uniform temperature of -10°C in a cryogenic cell (CellDyM, Calonne et al. (2015)). Each scan, consisting of
124 1440 2D radiographs, was reconstructed to obtain 3D grayscale images representing the attenuation coefficients of the different
125 materials composing the samples. The grayscale images were then transformed into binary (ice matrix – pore space) segmented
126 images using an energy-based segmentation algorithm (Hagenmuller et al., 2013).

127 **2.1.3 Cone Penetration Test (CPT)**

128 After the initial micro-tomography scan, a CPT was performed on the snow samples using a modified SnowMicroPenetrometer
129 (SMP version 4, Schneebeili and Johnson, 1998). The specific rod used by Peinke et al. (2020) displays a conic tip with an
130 apex angle α of 60° and a maximum cone radius equal to the rod radius R of 2.5 mm. The rod was inserted vertically into the
131 snow sample at a constant penetration speed v of 20 mm s^{-1} . The resisting force applied on the penetrometer (cone and rod)
132 was recorded at every $4\text{ }\mu\text{m}$ of penetration increment (i.e., 5 kHz frequency). The SMP sensor (Kistler sensor type 9207) can
133 measure forces up to 40 N with a resolution of 0.01 N. The tip was stopped at depths between 7 and 15 mm, i.e., 5 to 13 mm
134 above the sample bottom, to avoid boundary effects (Peinke et al., 2020). The experimental force profiles are presented in
135 Figure S26.

136 **2.2 Numerical modelling**

137 Snow is here considered as a granular cohesive material. The high strain rate ($> 10^{-4}\text{ s}^{-1}$) induced by the tip penetration in the
138 snow sample is considered to lead to brittle deformations, with inter-granular damage and grain rearrangements (Narita, 1983;
139 Johnson and Hopkins 2005; Hagenmuller et al., 2015). We adopted an approach based on DEM to simulate the cone penetration
140 tests in the measured snow samples. The mechanical model, based on YADE software (Šmilauer et al., 2015), is adapted from
141 the work of Hagenmuller et al. (2015) and Mede et al. (2018a, b and 2019).

142 The setting-up of the simulations involves different steps, namely the generation of the initial conditions based on measured
143 snow microstructures, the definition of the contact laws between the snow grains, and the setting of the boundary conditions
144 to reproduce the CPT configuration.

145 **2.2.1 Grain segmentation and grain shape representation**

146 The DEM model was fed by the 3D ice-air images derived from μCT . The continuous ice matrix was first segmented into
147 individual grains based on geometrical criteria, as described by Hagenmuller et al. (2013). The main idea of the approach is
148 to detect potential mechanical weakness zones (i.e., the bonds) based on the principal minimal curvature κ_T and a contiguity
149 parameter c_T . The threshold on curvature κ_T was set to 1.0 for RG, RGl_r and DH samples and to 0.7 for PP sample; the contiguity
150 parameter was set to 0.1 for all the samples (see Hagenmuller et al., 2013 for details).

151 To construct the DEM sample, the irregular shape of the grains was approximated by filling the grain volume with a population
152 of overlapping spheres (Fig. 1). The position of these spheres was derived from the medial axis of the structure (Coeurjolly et
153 al., 2007; Mede et al., 2018a) and redundant spheres were discarded based on a power diagram filter (Coeurjolly et al., 2007).

154 This grain shape representation by a multitude of spheres preserves the capability of YADE to handle sphere-sphere contact
155 detection. However, a high number of spheres slows down the simulations. We thus further decimated the number of spheres
156 by approximating the grain shape. We only selected the spheres with a radius larger than a threshold L (voxel) and with a
157 relative coverage larger than S (i.e., the ice volume associated with the sphere according to the power diagram should be larger
158 than S times the sphere volume (Coeurjolly et al., 2007). A trade-off must be found between this grain shape approximation,
159 influencing the simulation accuracy, and the number of spheres influencing the numerical cost. Eventually, the spheres
160 belonging to the same grain were clumped together in rigid aggregates constituting single discrete elements (DE). A detailed
161 sensitivity analysis was conducted (see supplementary material, Table S1 and Fig. S1) to determine the optimal values of L
162 and S parameters. Note that this grain shape approximation might also lead to delete the smallest grains in the numerical
163 samples, as they cannot be covered with the chosen parameters L and S . The grain number difference and shape approximation
164 of the numerical sample compared to initial the segmented μ CT image can be quantified by computing the volumetric error
165 E_V . The final chosen L and S values for each snow type, with the associated volumetric E_V and mechanical E_M errors (defined
166 in Sect. S1.1), can be found in Table 1.

167

| Sample name | Snow type | Sieve size (mm) | Bulk density (kg m ⁻³) | SSA (m ² kg ⁻¹) | L (vx) | S | Number of spheres | Number of grains | Number of initial cohesive interactions between grains | Initial contact density ν | E_V (%) | E_M (%) |
|-------------|------------------------|-----------------|------------------------------------|--|--------|-----|-------------------|------------------|--|-------------------------------|-----------|-----------|
| RG | Rounded Grains | 1.6 | 289 | 23.0 | 5 | 0.3 | 514917 | 27560 | 47736 | 0.55 | 42.3 | 5.3 |
| RGlr | Large Rounded Grains | 1 | 530 | 10.1 | 5 | 0.3 | 270143 | 8488 | 24005 | 1.63 | 14.6 | 4.2 |
| DH | Depth Hoar | 1.6 | 364 | 15.9 | 5 | 0.2 | 743546 | 11211 | 24258 | 0.86 | 24.7 | 14.3 |
| PP | Precipitation Particle | 1.6 | 91.3 | 53.5 | 2 | 0.5 | 1797567 | 95022 | 125805 | 0.13 | 32.2 | 10.3 |

168 **Table 1: Overview of the snow samples analysed in this study and parameters of DEM grain shape representation. Sample names**
169 **were given according to the snow type classification (Fierz et al., 2009). The sample density and specific surface area (SSA) were**
170 **derived from the micro-tomographic images (Peinke et al., 2020). The initial contact density was computed according to Eq. 10. The**
171 **minimum radius of the sphere L and the minimum sphere coverage S were determined through a sensitivity analysis presented in**
172 **Sect. S1.1. The resulting number of spheres, grains and cohesive grain-grain interactions are indicated, as well as the volumetric**
173 **error E_V and the mechanical error E_M associated with each grain shape representation.**

174

175 2.2.2 Interactions and contact law

176 The contacts between adjacent grains were identified during the grain segmentation phase. In the DEM simulations, each grain
177 contact is represented by several sphere-sphere interactions. The interactions between spheres are described by an elastic brittle

178 cohesive contact law characterised by four parameters, namely the normal and the shear contact stiffness K_N and K_S , the
 179 adhesion A , and the friction angle φ . The normal force F_N between two spheres is computed as proportional to the distance
 180 between the two sphere surfaces x_N , and limited by the adhesion value in the tensile regime ($x_N > 0$):

$$181 \quad F_N = K_N x_N \leq A. \quad (1)$$

182 The shear force F_S is proportional to the shear displacement between the spheres x_S , with a maximal value given by the sum
 183 of adhesion and friction:

$$184 \quad F_S = K_S x_S \leq A + F_N \tan(\varphi). \quad (2)$$

185 If the force exceeds the threshold, either in tension or in shear, the cohesive bond is broken. As long as the spheres remain in
 186 contact after the bond is broken, friction remains active in shear. In the initial state, all interactions in the numerical sample
 187 are considered cohesive. While the sample deforms, grain displacements lead to progressive breakage of the initial cohesive
 188 interactions and the potential creation of new contacts. These new interactions are frictional only (no cohesion), meaning that
 189 sintering mechanisms are not considered in this study.

190 The force of a given intergranular cohesive contact corresponds to the sum of all the associated sphere-sphere interactions.
 191 Based on the total contact surface between two grains (obtained from the μ CT image) and the number of associated sphere-
 192 sphere interactions, each sphere-sphere interaction i can be associated with a representative contact surface D_i . In order to
 193 recover the correct cohesion strength between two grains, the adhesion parameter A was defined for each sphere-sphere
 194 interaction as:

$$195 \quad A_i = D_i C, \quad (3)$$

196 with C (Pa) the cohesion of ice. In YADE, by default, the contact stiffnesses are computed based on the radii of the spheres in
 197 interaction and two elastic material parameters, namely the Young's modulus E and the Poisson ratio ν . For our computations,
 198 to ensure that all cohesive sphere-sphere interactions between two grains break at the same separation distance, the computation
 199 of the normal stiffness was redefined as:

$$200 \quad K_{N,i} = \frac{D_i E}{r_{mean}}, \quad (4)$$

201 where r_{mean} (m) is a characteristic length constant for all the interactions in the numerical sample, taken as the mean sphere
 202 radius. The shear stiffness is then defined as:

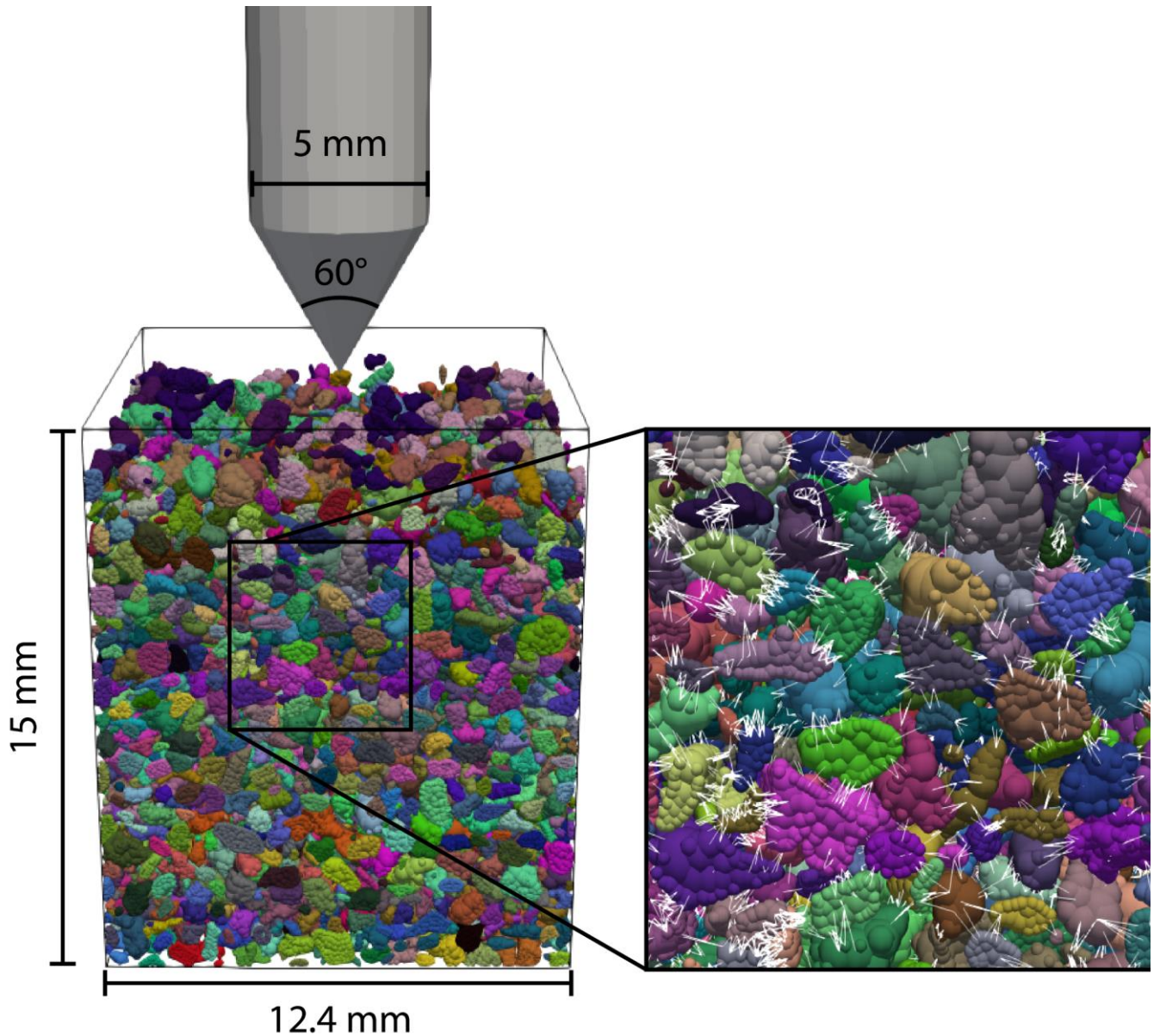
$$203 \quad K_S = \nu \times K_N. \quad (5)$$

204 Note that due to the rather arbitrary characteristic length considered in the definition of the normal stiffness [Eq. (4)], which
 205 depends on the grain shape approximation, as well as to the simple linear relation considered for the normal force [Eq. (1)],
 206 the contact-level YADE Young's modulus E should not be regarded as the "true" Young's modulus of the material, but rather
 207 as a representative parameter of the elastic properties at the contacts.

209 **2.2.3 Simulation setup and critical time step**

210 In order to evaluate the DEM model, we have implemented a CPT configuration similar to the experimental setup used by
211 Peinke et al. (2020) (Fig. 1). The snow sample is contained in a rectangular box open at the top. The box is about 12.4 mm
212 along the x- and y-axis and about 15 mm along the z-axis. The vertical and horizontal box sizes were reduced compared to the
213 20 mm height and 20 mm diameter respectively of the sample holder used by Peinke et al. (2020). This choice has been
214 motivated by (1) simplifying the geometry with a rectangular numerical sample, (2) matching the sample height imaged with
215 μ CT and (3) reducing the computational time. A sample size sensitivity analysis has been performed to ensure that border
216 effects are not introduced by reducing the sample size (Fig. S2). The penetrometer tip displays a maximal radius R of 2.5 mm
217 and an apex angle α of 60° . Initially in a centered position at the box surface, it is displaced downwards through the sample at
218 a constant speed of 20 mm s^{-1} . The simulation stops when the tip reaches the bottom of the box. The walls (box and tip) are
219 represented by facets with rigid boundary conditions. The gravity is set to 9.81 m s^{-2} .

220



221
222
223
224

Figure 1: Illustration of DEM CPT modelling for the RGlR sample. The penetrometer is moving downward at a constant speed of 20 mm s^{-1} . Snow grains (represented with different colours) are modelled by overlapping spheres clumped together. The zoomed window shows the initial cohesive interactions between the spheres of adjacent grains (white lines).

225

226 The stability of the explicit integration scheme is ensured by estimating the critical time step, based on the propagation speed
227 of elastic waves in the sample (Zhao, 2017):

228
$$\Delta t_{cr} = \min \left(\frac{m_i}{K_{N,i}} \right)^{0.5}, \quad (6)$$

229 with m_i and $K_{N,i}$ the mass and normal stiffness of the DE i . The mass m_i or, equivalently the material density ρ , can be artificially
 230 increased to increase the time step (Hagenmuller et al., 2015). A numerical sensitivity analysis (Fig. S3) has shown that
 231 increasing the density by a factor f equal to 100 does not affect the simulation results, while significantly reducing the
 232 computing time. Finally, a Cundall's non-viscous damping coefficient Λ was applied to the particle acceleration to dissipate
 233 kinetic energy and avoid numerical instabilities (Šmilauer et al. 2015). A value of 0.05 was chosen according to the results of
 234 a numerical sensitivity analysis (Fig. S4).

235 2.2.4 Input parameters

236 In view of the preceding paragraph, the density of the ice grains was set to $\rho = f \times 917 \text{ kg m}^{-3}$. The contact law parameters were
 237 derived from typical values measured on ice. The Poisson coefficient P was set to 0.3 (Schulson and Duval, 2009). The typical
 238 Young's modulus E , the cohesion strength C and the friction coefficient $\tan(\varphi)$ values for the ice are usually evaluated around
 239 $1 \times 10^{10} \text{ Pa}$, $1 \times 10^6 \text{ Pa}$ and 0.2, respectively (Gammon et al., 1983; Schulson and Duval, 2009). For this study, a sensitivity
 240 analysis to the values of these parameters was performed to get insights into their influence and best adjust simulation results
 241 to the experimental measurements. The considered ranges were 1×10^8 - $1 \times 10^{10} \text{ Pa}$ for E , 5×10^5 - $5 \times 10^6 \text{ Pa}$ for C and 0.2-0.5
 242 for $\tan(\varphi)$, respectively. Note that the range of the Young's modulus E ensures small grain overlaps, i.e. compliance with the
 243 rigid grain assumption (Fig. S5). We must mention that, due to longer computing times, fewer parameter values could be
 244 explored for large Young's modulus values. For the PP sample, no numerical simulations could be performed for a Young's
 245 modulus of $1 \times 10^{10} \text{ Pa}$, as computing times were unreasonable ($E = 1 \times 10^8 \text{ Pa}$, $t \sim 4$ months and $E = 1 \times 10^9 \text{ Pa}$, $t \sim 10$ months
 246 on a 72 cores machine with 2.6 GHz Intel Xeon processors (2.6 GHz) and 500 GB RAM. YADE scripts enable parallelisation
 247 on up to 5 cores).

248

| Simulation setup | | |
|---------------------------------|-----------------|--|
| Sample width | W | 13 mm |
| Sample height | H | 15 mm |
| Tip radius | R | 2.5 mm |
| Cone apex | a | 60° |
| Tip velocity | v | 20 mm s^{-1} |
| Gravity | g | 9.81 m s^{-2} |
| Numerical parameters | | |
| Time step | dt | $\sim 1 \times 10^{-6}$ - $1 \times 10^{-8} \text{ s}$ |
| Mass factor | f | 100 |
| Non-viscous damping coefficient | Λ | 0.05 |
| Material properties | | |
| Grain density | ρ | $917 \times 10^2 \text{ kg m}^{-3}$ |
| Poisson coefficient | P | 0.3 |
| Friction coefficient | $\tan(\varphi)$ | 0.2–0.5 (default value 0.2) |
| Young's modulus | E | 1×10^8 – 1×10^{10} (default value 1×10^9) Pa |
| Cohesion | C | 5×10^5 – 5×10^6 (default value 2×10^6) Pa |

249 **Table 2: Input parameters used for the simulations presented in this paper.**

251 **2.3 Data processing**

252 The outputs of the DEM simulations are the resisting force exerted by the grains on the penetrating rod and the displacement
253 of the grains. These results can be directly compared to the experimental measurements.

254 **2.3.1 Force sampling**

255 The sum of the forces along the z-axis applied on all the facets constituting the penetrometer (cone and rod) is recorded at each
256 time step. The characteristics of the raw numerical force profiles depend on the numerical parameters (notably the time step),
257 and are not necessarily suited for direct comparison with experimental results. To obtain numerical profiles that can be
258 compared to their experimental counterparts, the simulated force values were averaged over windows corresponding to
259 displacement increments of 4 μm , thus matching the sampling frequency of the SMP. This averaging is also useful to smooth
260 out high-frequency fluctuations linked to the very small time steps used in DEM. Finally, numerical and experimental force
261 profiles are then re-sampled by linear interpolation over a regular grid with a step of 4 μm over the same depth. The profiles
262 span from a depth of 0 mm (initial contact between the cone and the sample surface) to the chosen maximum depth, which, in
263 our study, is set to 7 mm (i.e., 1750 points). This value corresponds to the minimum depth reached by the penetrometer during
264 the experimental CPT tests for the selected samples.

265 **2.3.2 Statistical indicators**

266 Quantitatively, the DEM numerical model is evaluated by comparisons with experimental force profiles in terms of three
267 statistical indicators: the mean macroscopic force \bar{F} (N), the amplitude of force fluctuations σ (N), and the correlation length l
268 (mm). The indicator σ is calculated as the variance of the detrended force profile as follows:

$$269 \sigma = \sqrt{\tilde{F}^2}, \quad \tilde{F} = \frac{F - F_{sm}}{F_{sm}} \quad (7)$$

270 with \tilde{F} ([Eq. (5)], Peinke et al. 2019), the detrended force profile, F , the force profile and F_{sm} , the averaged force profile
271 calculated over a rolling window $\Delta z = 3$ mm. The correlation length l (mm) is also computed on the detrended force profile
272 (Peinke et al. 2019). In our study, the snow samples exhibit a rather homogeneous structure allowing us to consider that l is
273 constant over the depth (Peinke et al., 2019). These three statistical indicators have been chosen because they are easily
274 quantifiable and commonly used to describe force profiles obtained by CPT in snow (Johnsson and Schneebeli, 1999; Löwe
275 and van Herwijnen, 2012; Peinke et al. 2019). In addition, they constitute key parameters to derive additional microstructural
276 properties based on Poisson shot noise models (Löwe and van Herwijnen, 2012; Peinke et al. 2019).

277 To select the set of model mechanical parameters (E , C and $\tan(\varphi)$) providing the best fit to the experimental measurements, a
278 total error RE_{tot} is computed according to:

$$RE_{tot} = \sqrt{2 RE_F^2 + RE_\sigma^2 + RE_l^2} \quad (8)$$

with RE_k the logarithmic relative error calculated for the three statistical indicators, $k = (F, \sigma, l)$, as:

$$RE_k = \frac{\log(\text{measured value}_k) - \log(\text{computed value}_k)}{\log(\text{measured value}_k)} \quad (9)$$

Given the difficulties in reproducing the correlation length with the DEM model for two out of four samples and the fact that the values of the statistical indicators vary over several orders of magnitude (see Section 3.2), the logarithmic relative errors RE_k were computed with the log of the considered values. We have attributed a weight factor of 2 to the logarithmic relative error RE_F related to the mean macroscopic force, to put more emphasis on the correct reproduction of this quantity. Hence, for each snow sample, the set of mechanical parameters minimising the total error RE_{tot} was determined.

2.3.3 Grain displacement analysis

The position of all grains was recorded every ~ 0.4 mm of penetration in the DEM simulations. The total displacements and the trajectories can therefore be reconstructed for each grain. Due to the thermodynamically active nature of snow, interrupted experimental tests were not feasible and only the initial (before CPT) and the final states (after CPT) of the snow sample could be imaged by μ CT. Grain tracking, applied to the micro-tomographic images, has been performed by Peinke et al. (2020), providing the total displacement of the identified grains. We thus compared the total displacement between the CPT experiments and the DEM simulations at the same penetration depth, i.e., at the maximal penetration measured experimentally. Note that grain tracking could not be performed for the PP sample due to the small size of the grains.

The profiles of vertical and radial displacements were averaged around the cone axis and over the height of an area located between the top section of the cone and the sample surface. A displacement threshold of 0.03 mm was set to define the CZ (Peinke et al., 2020). Only the radial profiles were compared to the experimental results, as we suspect the vertical profiles derived from μ CT scans might be misleading (Peinke et al. 2020). Indeed, before acquiring the post-CPT μ CT scans, the tip was removed from the snow. This procedure was performed about one hour after the tip penetration, to allow for bonds between ice grains to re-form by sintering and limit grain displacements during tip removal. However, despite this precaution, some grains in contact with the tip might have been dragged upward due to friction with the tip. Therefore, the upward component of the vertical displacement might have been overestimated in the experimental results, especially for the larger grains.

3 Results

3.1 Simulated Cone Penetration Tests

This section presents an example of CPT simulation results for the case of the RG snow sample with the following mechanical parameters: $E = 1 \times 10^9$ Pa, $C = 5 \times 10^6$ Pa and $\tan(\varphi) = 0.2$ (Table 3). The results for the other snow samples are shown in

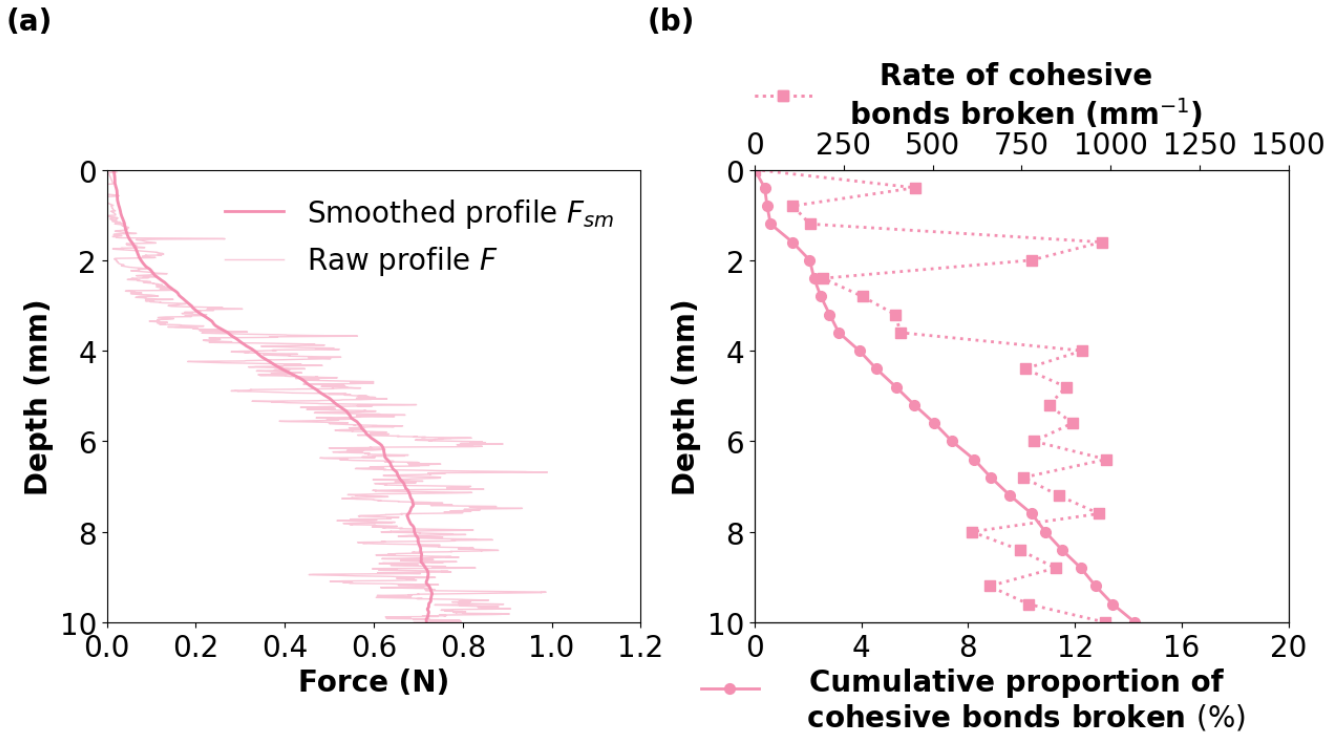
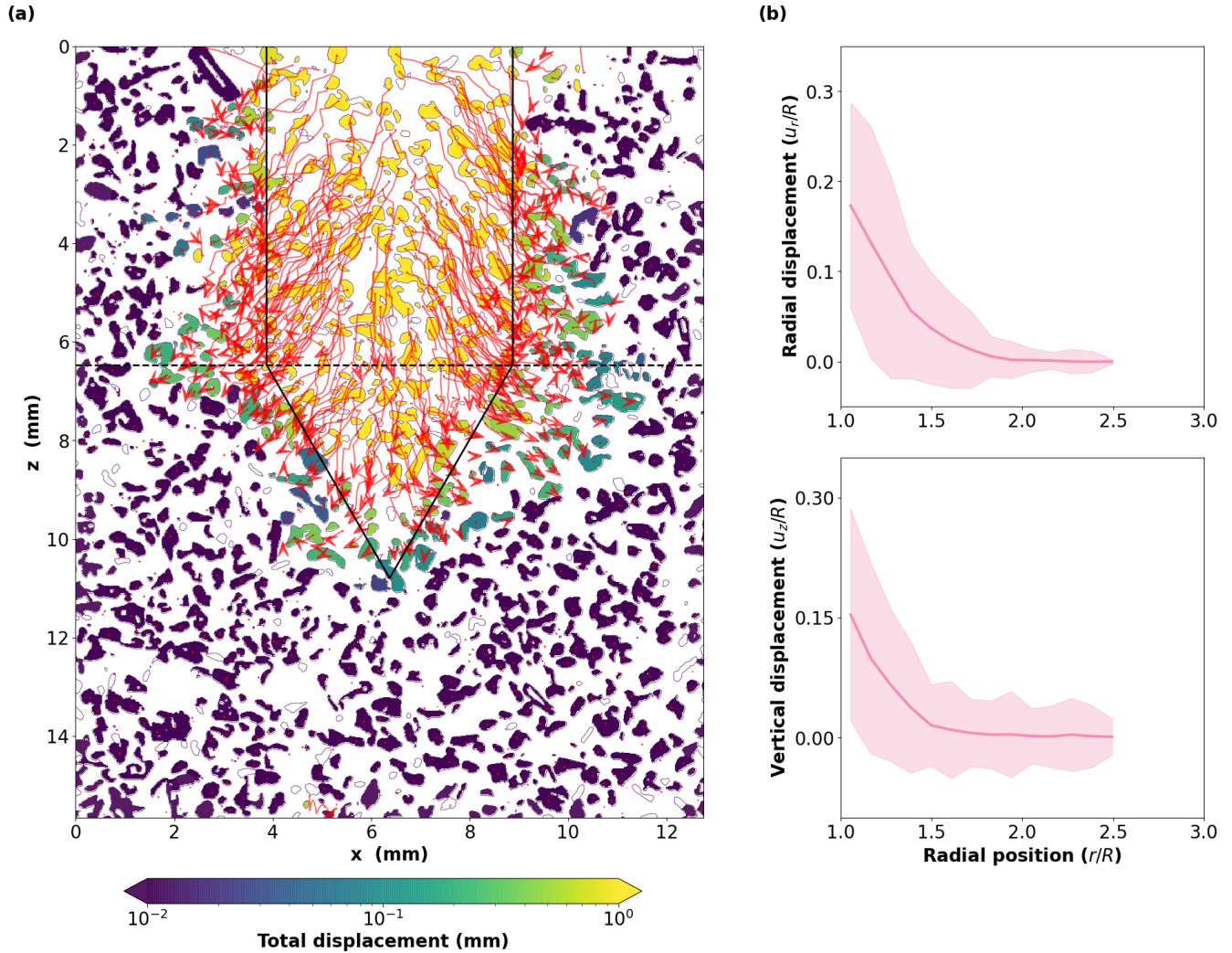


Figure 2: (a) Force F as a function of penetration depth (light line) obtained for the RG sample. The superposed smoothed profile (bold line) F_{sm} corresponds to the force value averaged over a rolling window of 3 mm. (b) Rate of cohesive bonds broken per unit penetration depth and cumulative proportion of cohesive bonds broken (%) as a function of tip penetration depth. The initial number of cohesive bonds is indicated in Table 1. The results are obtained with the mechanical parameters indicated in Table 3.

The simulated penetration force globally increases with depth and is characterised by high-frequency fluctuations whose amplitude also tends to increase with depth (Fig. 2 (a)). The force profile displays an ‘S’ shape with three stages: 1) up to ~ 3.5 mm depth, the profile is convex, 2) between ~ 3.5 and ~ 6 mm depth, the increase of force with depth is almost linear, and 3) for depths larger than 6 mm, the force reaches a nearly constant value. A similar behaviour is observable for the RGIr and PP samples (Fig. S6 (a) and S10 (a)), with slight variations in the transition depths between the different stages. For the DH sample, the macroscopic force profile also displays stages 1 and 2, but the stabilisation at a nearly constant value is less evident for the results presented in Fig. S (a). Stage 3 might be reached at greater depths for this sample.

The penetration of the tip induces bond failures in the simulated samples (Fig. 2 (b)). Overall, for the RG sample, about 15% of the cohesive interactions broke over 10 mm of penetration, corresponding to an average rate of ~ 650 bond failures mm^{-1} . This average bond failure rate is variable among the samples, reaching up to 1400 bond failures mm^{-1} for RGIr sample (Figs. S6 (b), S8 (b), S10 (b)). In detail, for the RG sample, we notice an increase in the bond failure rate at around 3.5 mm of

326 penetration depth (Fig. 2 (b)), coinciding with the transition between the first and second stages observed in the force signal
 327 (Fig. 2 (a)). Bond failure intensity then remains nearly constant as the macroscopic force reaches its steady-state value. Similar
 328 characteristics are observed for the other snow types (Figs. S6, S10) except for the DH sample, for which the slope change
 329 between the first and second stages is less clear (Fig. S8 (b)).
 330



331
 332 **Figure 3: (a) Simulated grain displacement map for the RG sample. The red arrows indicate the grain trajectories while the tip is**
 333 **penetrating (sampling = 0.4 mm). White grains correspond to grains that are not represented in the DEM simulation. The final tip**
 334 **position is indicated by the black solid lines. The horizontal black dashed line indicates the cone top. (b) Radial (upper panel) and**
 335 **vertical (lower panel) displacement profiles (red curves) for the RG sample. These profiles represent averages computed from the**
 336 **sample surface to the cone top. By convention, downward (respectively upward) movement corresponds to positive (respectively**
 337 **negative) values of vertical displacement. The shadowed areas around the solid lines represent the standard deviation of grain**
 338 **displacements. The results are obtained with the mechanical parameters indicated in Table 3.**

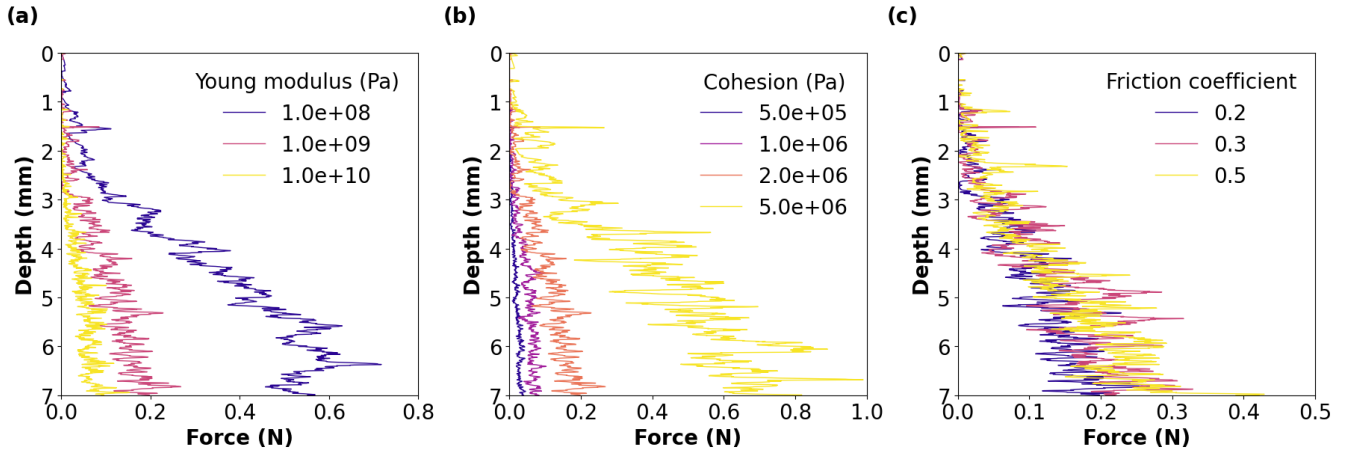
339

340 Figure 3 (a) shows the total displacement of the grains as well as grain trajectories. The largest displacements (up to several
 341 mm) are observed for grains initially located on the path of the tip. Around the tip, the displacements are < 1 mm and are
 342 mainly localised close to the tip. Grain trajectories indicate that grains are pushed downward from each side of the tip. Grains
 343 initially located on the tip axis display quasi-straight vertical trajectories. The trajectories become more radial and curved away
 344 from the tip medial axis, with grains also being pushed aside. Both radial and vertical displacement profiles show a pronounced
 345 decreasing trend and reach almost zero values at a radial position of about 1.7 - $1.8R$ (Fig. 3 (b)). The vertical profile attests of
 346 a dominant downward movement of the grains close to the tip. Similar observations are made for the DH (Fig. S9) and PP
 347 (Fig. S11) samples. In contrast, for the RGIr sample, vertical displacements are smaller and oriented slightly upward on
 348 average, for the mechanical parameters chosen here (Fig. S7).

349 3.2 Sensitivity to mechanical parameters

350 The influence of the mechanical parameters (Young's modulus, cohesion, friction coefficient) involved in the contact law has
 351 been systematically explored. For the RG sample, the force profiles obtained for the different values of the parameters within
 352 the explored ranges (Table 2) are presented in Figure 4, and synthetic plots of the sensitivity of the statistical indicators to
 353 these parameters are presented in Figure 5. The results for the other snow samples can be found in Sect. S2.3. Table S3 also
 354 summarises the values of statistical indicators in all cases.

355



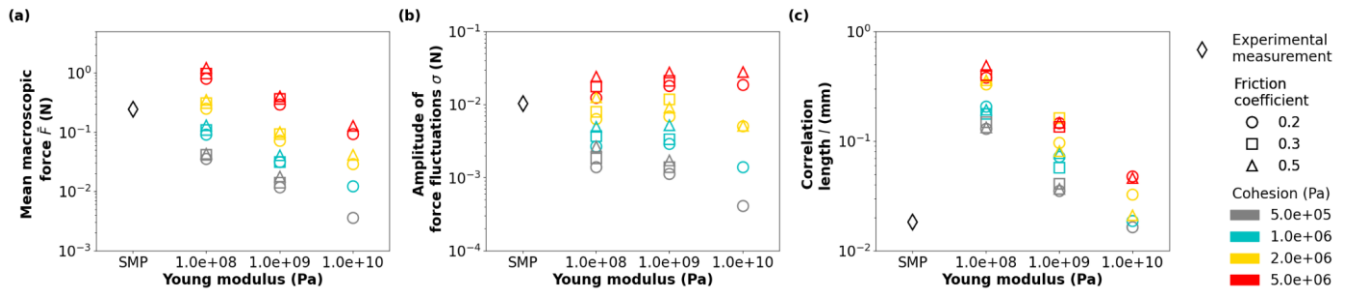
356

357 **Figure 4: Influence of mechanical parameters on the simulated force profile. The sensitivity analysis has been performed on (a)**
 358 **Young's modulus E (Pa) (for $C = 2.0 \times 10^6$ Pa and $\tan(\varphi) = 0.2$), (b) cohesion C (Pa) (for $E = 1.0 \times 10^9$ Pa and $\tan(\varphi) = 0.2$), and (c)**
 359 **friction coefficient $\tan(\varphi)$ (for $E = 1.0 \times 10^9$ Pa and $C = 2.0 \times 10^6$ Pa). The results presented here correspond to the RG sample.**

360

361 First, it can be observed that increasing Young's modulus decreases the mean macroscopic force (Figs. 4 (a) and 5 (a)) and the
 362 correlation length (Fig. 5 (c)). The influence of Young's modulus on the amplitude of force fluctuations is more complex and

363 displays a co-dependency with the cohesion values (Fig. 5 (b)). For low (respectively high) cohesion values, the amplitude of
 364 force fluctuations shows a decreasing (respectively increasing) trend with Young's modulus. Regarding the influence of
 365 cohesion, it is observed that increasing this parameter increases the three statistical indicators. Finally, increasing the friction
 366 coefficient, generally also leads to an increase of the three statistical indicators. Note however that, over the range of explored
 367 friction coefficient values (0.2-0.5), the sensitivity to this parameter is less important than for the other two mechanical
 368 parameters (where E is varied over two orders of magnitude and C is varied over one order of magnitude). Despite changes in
 369 absolute force values, the evolution of the force profiles (Figs. S14, S18 and S22) and statistical indicators (Figs. S15, S19 and
 370 S23) with the mechanical parameters follow similar trends for all the samples.
 371



372
 373 **Figure 5: Evolution of statistical indicators as functions of Young's modulus, cohesion and friction coefficient: (a) Mean macroscopic**
 374 **force \bar{F} , (b) amplitude of force fluctuations σ , and (c) correlation length l . The experimental results (black diamonds) are also**
 375 **represented in the plots. The results presented here correspond to the RG sample.**

376
 377 The number of broken bonds per increment of tip penetration depth appears rather insensitive to Young's modulus (Figs. S12
 378 (a), S16 (a), S20 (a), S24 (a)) and is only slightly reduced when cohesion increases (Figs. S12 (b), S16 (b), S20 (b), S24 (b)).
 379 Conversely, this quantity is significantly affected by the friction coefficient, with an increase of the average bond failure rate
 380 when $\tan(\phi)$ increases (Figs. S12 (c), S16 (c), S20 (c), S24 (c)).

381 Finally, it is observed that the influence of the mechanical parameters on the radial grain displacement profiles is negligible
 382 (Figs. S13, S17, S21, S25). Young's modulus shows no influence on the vertical grain displacement either. Cohesion appears
 383 to play a role in the vertical displacement profile for the RGIr sample, by enhancing upward movements. Larger friction
 384 coefficients tend to increase the downward movement of the grains close to the tip for all the snow types.

385 3.3 Comparison of DEM results with experimental measurements

386 A first noticeable observation is that, for the values of the mechanical parameters tested, the orders of magnitude of the
 387 statistical indicators obtained numerically are consistent with the experimental results in most of the cases (Figs. 5, S15, S19,
 388 S23, Table S2, Table S3). This demonstrates that the DEM model is indeed capable of reproducing the main characteristics of
 389 the CPT force profile (Fig. S26, Table S2). However, we highlight the difficulty of matching the three statistical indicators at
 390 once for a given combination of the three mechanical parameters studied. Hence, for the RG sample (Fig. 5), the DEM

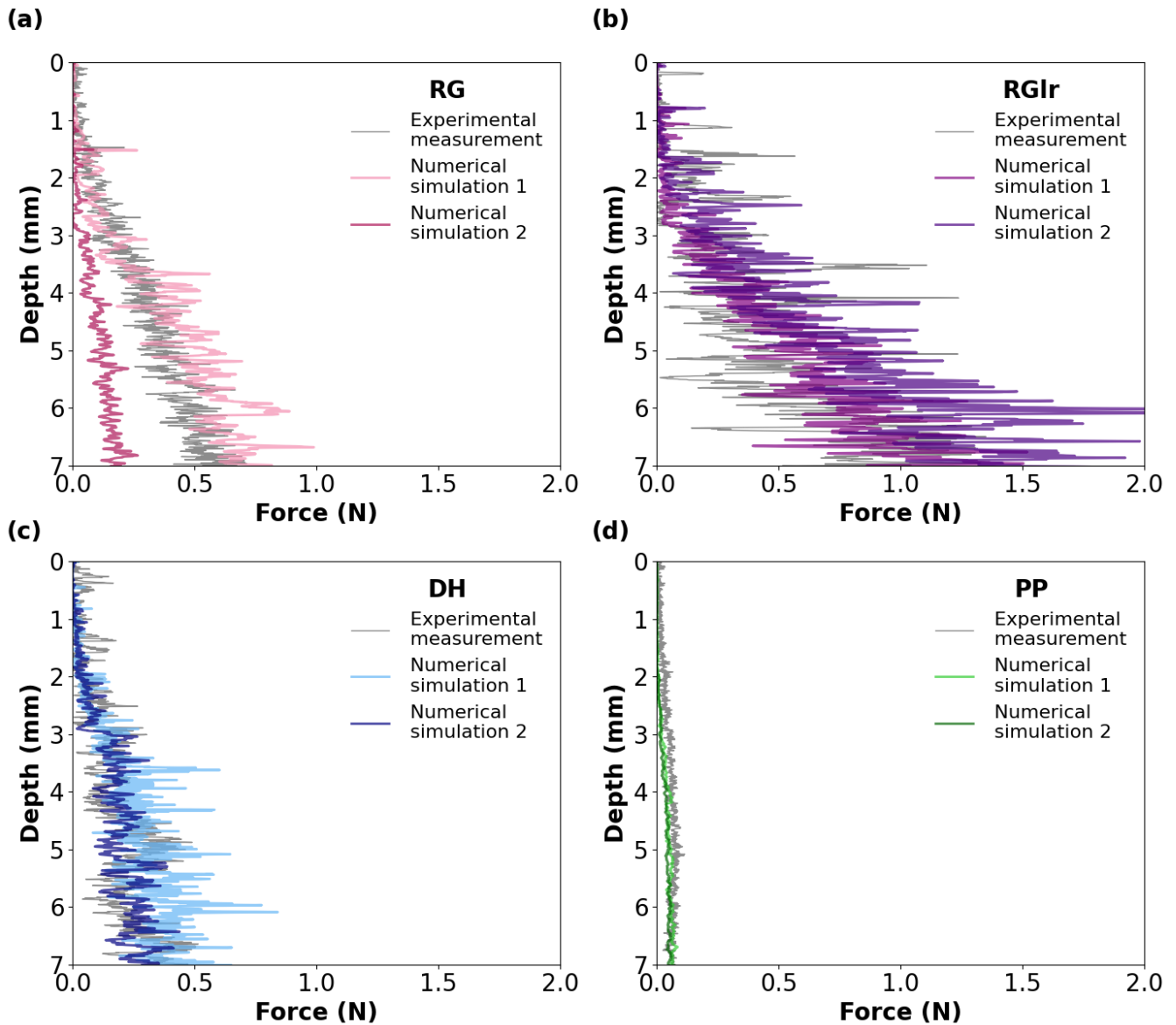
391 simulation can reproduce the experimental mean macroscopic force and the amplitude of force fluctuations but tends to
 392 overestimate the correlation length by a factor of 8 for the best combination of mechanical parameters. For the RGl_r and DH
 393 samples (Figs. S15, S18), all the experimental statistical indicators can be reproduced individually, but not for one single
 394 combination of the mechanical parameters. For the PP sample, the experimental mean macroscopic force and the amplitude of
 395 force fluctuations can be reproduced numerically, but the correlation length is systematically overestimated by a factor of at
 396 least 8 (Fig. S23).

| Sample | E (Pa) | C (Pa) | tan(ϕ) | RE _F | RE _{σ} | RE _l | RE _{tot} |
|------------------------|----------------------|---------------------|---------------|-------------------------|-----------------------------------|-------------------------|------------------------|
| RG | 1 x 10 ⁹ | 5 x 10 ⁶ | 0.2 | 1.2 x 10 ⁻¹ | 1.2 x 10 ⁻¹ | 5.2 x 10 ⁻¹ | 5.6 x 10 ⁻¹ |
| RGl_r | 1 x 10 ⁹ | 1 x 10 ⁶ | 0.3 | 5.5 x 10 ⁻² | -4.6 x 10 ⁻¹ | 1.1 x 10 ⁻¹ | 4.8 x 10 ⁻¹ |
| DH | 1 x 10 ¹⁰ | 5 x 10 ⁶ | 0.2 | 1.2 x 10 ⁻¹ | -1.1 x 10 ⁻¹ | -2.3 x 10 ⁻¹ | 3.1 x 10 ⁻¹ |
| PP | 1 x 10 ⁹ | 2 x 10 ⁶ | 0.5 | -1.3 x 10 ⁻¹ | -1.6 x 10 ⁻¹ | 6.5 x 10 ⁻¹ | 6.9 x 10 ⁻¹ |

398 **Table 3: Selected combination of mechanical parameters for RG, RGl_r, DH and PP samples. The indicated values of Young's**
 399 **modulus E , cohesion C and friction coefficient $\tan(\phi)$ correspond to the combinations that yield the lowest total error RE_{tot} on the**
 400 **statistical indicators (mean macroscopic force \bar{F} , amplitude of force fluctuations σ , correlation length l) measured experimentally.**
 401 **Logarithmic relative error RE_k for all the mechanical parameter combinations tested are indicated in Table S3.**

402
 403 Based on the sensitivity analysis (Sect. 3.2.3.), we selected for each sample the combination of the three mechanical parameters
 404 that minimises the total error RE_{tot} (Tables 3, S3). The corresponding simulated force profiles (referred to as ‘Numerical
 405 simulation 1’) are compared with the experimental profiles in Fig. 6. Note that the error values quoted in the text below
 406 correspond to relative errors calculated without the logarithmic function, as they are easier to grasp. These values therefore
 407 differ from the logarithmic relative errors shown in Tables 3 and S3 and used for the parameter selection. From a qualitative
 408 point of view, a good overall agreement is observed between these numerical and experimental force profiles. For the RG
 409 sample, the experimental mean macroscopic force is overestimated by ~20% by the numerical result, the amplitude of force
 410 fluctuation is overestimated by ~70% and the correlation length is largely overestimated by a factor of 8 (Figs. 5, 6 (a), Table
 411 3). Both the experimental and numerical force profiles reach a quasi-steady-state value at about the same depth (~6 mm, S27).
 412 For the RGl_r sample, the experimental mean macroscopic force is fairly reproduced with a relative error of 6%, the amplitude
 413 of force fluctuations is underestimated by ~60% and the correlation length is overestimated by 35% (Figs. S15 and 6 (b),
 414 Table 3). We note that the slope change between 2.5 and 3 mm penetration depth is reproduced numerically. However, it
 415 appeared difficult to reproduce numerically the amplitude of force fluctuations in the upper section (from 0 to 4 mm) of the
 416 experimental profile. For the DH sample, the experimental mean macroscopic force is overestimated by ~25%. The
 417 experimental amplitude of force fluctuations is underestimated by 28% and the correlation length is about half of the
 418 experimental value (Figs. S19, 6 (c), Table 3). The numerical results minimise the force peaks observed in the upper part of
 419 the experimental profile (above 3 mm) but reproduce fairly well the main features of the amplitude of force fluctuations,
 420 especially the force “jump” at 3 mm depth. Finally, for the PP sample, the experimental mean macroscopic force is
 421 underestimated by ~30%, while the experimental amplitude of force fluctuations is underestimated by ~60%. In this case, the

422 experimental correlation length could not be reproduced at all, with values overestimated by a factor of 20 (Figs. S23 and 6
423 (d), Table 3).
424

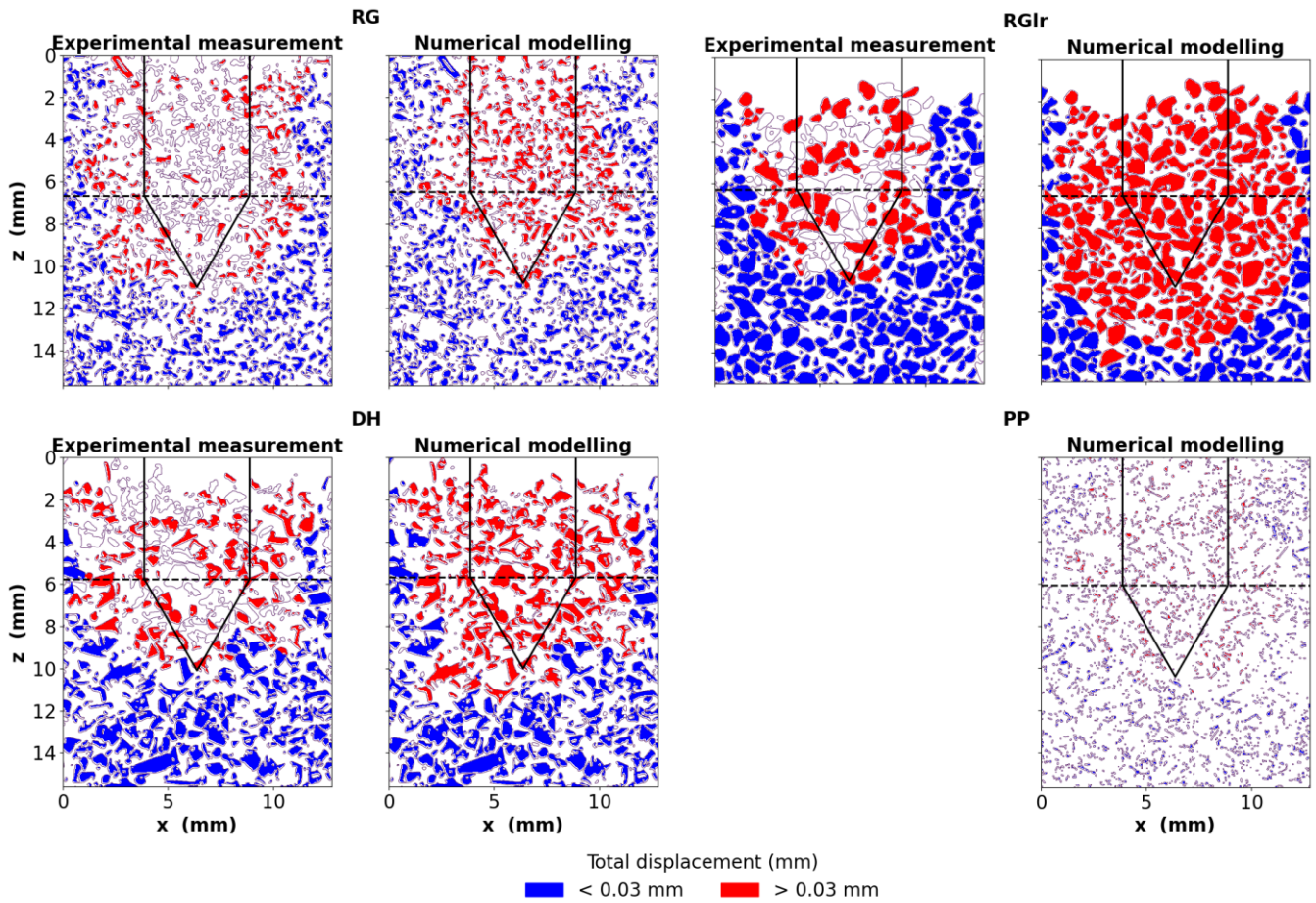


425
426 **Figure 6: Experimental (grey) and numerical (coloured) CPT force profiles obtained for (a) RG, (b) RGlR, (c) DH, and (d) and PP**
427 **samples. The “Numerical simulation 1” profiles correspond to the best fit of the mechanical parameters determined for each sample**
428 **(Table 3), while “Numerical simulation 2” profiles correspond to an overall best fit of the mechanical parameters for the four**
429 **samples ($E = 1 \times 10^9$ Pa, $C = 2 \times 10^6$ Pa and $\tan(\varphi) = 0.2$, Table S3).**

430

431 For comparison, we also selected the single set of mechanical parameters that minimises the combined total error RE_{tot} on RG,
432 RGlR, DH and PP samples. Corresponding values are: $E = 1 \times 10^9$ Pa, $C = 2 \times 10^6$ Pa and $\tan(\varphi) = 0.2$. The respective
433 logarithmic relative errors for each sample can be found in Table S3. As before, the error values presented in the text below
434 correspond to the relative errors without the logarithmic function applied to the values. In general, the corresponding simulated
435 force profiles (referred to as ‘Numerical simulation 2’ in Fig. 6) also show a fair agreement with the experimental results. For
436 the RG sample, however, the experimental mean macroscopic force is significantly underestimated by $\sim 70\%$ (Figs. 5, 6 (a),
437 Table S3). The numerical amplitude of force fluctuations is underestimated by $\sim 35\%$, while the correlation length is
438 significantly overestimated by a factor of 5. For the RGlR sample, the agreement is acceptable for the three statistical indicators
439 with relative errors around 50%. For the DH sample, the experimental mean macroscopic force is reproduced at 90%, while
440 the experimental amplitude of force fluctuations is underestimated by 60% and the experimental correlation length is
441 overestimated by a factor of ~ 2 . Finally, for the PP sample, the experimental mean macroscopic force is underestimated by
442 $\sim 80\%$, the amplitude of force fluctuations by $\sim 85\%$ and the experimental correlation length is again strongly overestimated by
443 a factor of 20 (Figs. S23 and 6 (d), Table S3).

444



445

446

447

448

449

450

451

452

Figure 7: Total displacement maps obtained experimentally with μ CT (left panels) and numerically with DEM simulation (right panels) for the RG, RGlR, DH and PP samples. A displacement threshold of 0.03 mm has been set to define the deformation zone (Peinke et al., 2020). White grains correspond to non-trackable grains in μ CT scans (Peinke et al., 2020) and grains not represented in the DEM simulations. The final tip position is indicated with black solid lines. The horizontal black dashed line indicates the cone top. Displacement profiles shown in Fig. 8 are computed from the sample surface to the cone top. Numerical results are obtained with the mechanical parameters indicated in Table 3. The experimental displacement field could not be determined for the PP sample.

453

454

455

456

457

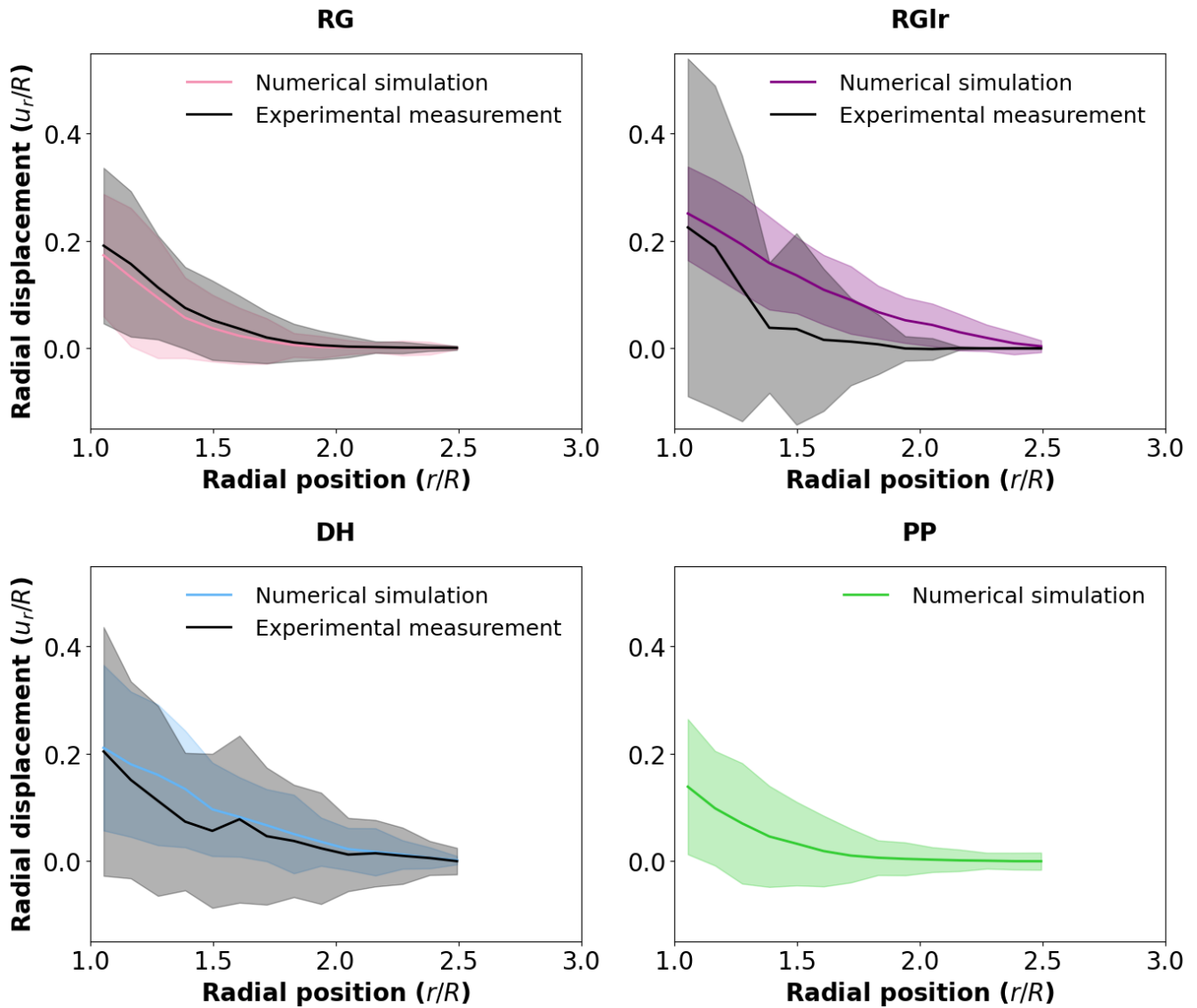
458

459

As shown in Fig. 7, the DEM simulations also proved capable of reproducing, at least qualitatively, the experimental grain displacement patterns derived from μ CT scans for the four snow types. Essentially similar results are obtained with the individual best-matching sets of mechanical parameters indicated in Table 3 (Fig. 7), and with the globally-matching set of parameters introduced in the previous paragraph (Fig. S28). For the RG sample, the overall shape and size of the deformation zone are well reproduced by the simulations. For the DH sample, the radial extension of the deformation zone is well reproduced by the simulations, but the vertical extension tends to be overestimated. The largest discrepancies are observed for

460 the RGl_r sample, for which the radial and vertical extensions of the deformation zone are overestimated compared to the
461 experimental data.

462



463

464

465

466

467

Figure 8: Radial displacement profiles (solid lines) obtained experimentally (black) and numerically (coloured) for the RG, RGl_r, DH and PP samples. The shadowed areas around the solid lines correspond to the standard deviation of grain displacement and exhibit the variability of the radial displacement of grains. The numerical results are obtained with the mechanical parameters indicated in Table 3.

468

469

470

Similarly, the radial displacement profiles obtained from the DEM numerical simulations are overall in good agreement with their experimental counterparts (Figs. 8 and S29). Consistently with the displacement maps, the largest discrepancy is observed

471 for the RGlR sample. In particular, the abrupt slope break seen in the experimental profile at a radial position of about 1.5 is
472 not reproduced in the numerical profile. Note however that, due to a relatively low number of trackable grains (Fig. 7), the
473 standard deviation of the grain radial displacements is larger in the experimental measurements, which may result in a larger
474 uncertainty on the average profile. In contrast, simulations on the RG and DH samples show a very good agreement with the
475 experiments. The CZ (defined with displacement threshold set at 0.03 mm) obtained from numerical simulations extends
476 radially up to $1.6R$, $2.2R$, $2.0R$ and $1.5R$ for the RG, RGlR, DH and PP samples, respectively. In comparison, the CZ derived
477 from μ CT scans extends radially up to $1.7R$, $1.5R$ and $1.9R$ for the RG, RGlR and DH samples, respectively (no measurement
478 for PP sample).

479 **4 Discussion**

480 **4.1 Evaluation of the DEM model**

481 We used three mechanical parameters, namely Young's modulus, the cohesion and the friction coefficient, to adjust the
482 simulated force profiles to the experimental results. Overall, the numerical model could reproduce relatively well the
483 mechanical response of all studied numerical samples with a single set of mechanical parameters ($E = 1 \times 10^9$ Pa, $C = 2 \times 10^6$
484 Pa and $\tan(\phi) = 0.2$) (Fig. 6), indicating that the differences in the force profiles among the samples are mainly dependent of
485 the snow microstructure.

486 It should also be noted that the values of the mechanical parameters obtained by adjusting the model on the experimental data
487 (either globally for all samples or for each sample individually, Table 3) are reasonably close to the mechanical properties of
488 ice. Young's modulus of ice is measured between 9×10^9 Pa and 10×10^9 Pa (Gammon et al., 1983), while our selected values
489 range between 1×10^9 Pa and 1×10^{10} Pa. Recall that, in YADE, the Young's modulus is a numerical parameter used to define
490 the normal contact stiffness, and is not expected to necessarily correspond to the physical Young's modulus of the material
491 (Sect. 2.2.2). Nevertheless, the fact that the numerical value of E is in the same range of magnitude as the elastic properties of
492 ice provides confidence that the DEM model and the used contact law ([Eqs. (1)-(5)]) correctly capture the physical processes
493 at play. Similarly, the numerical cohesion values, ranging between 1×10^6 Pa and 5×10^6 Pa, are in agreement with typical
494 cohesion values measured on ice (in the range 2×10^6 Pa to 6×10^6 Pa, Schulson and Duval, 2009). Finally, numerical friction
495 coefficients appear to be on the order of 0.2–0.5, while values measured experimentally generally range from 0.02 to 1 (Fish
496 and Zaretsky, 1997; Maneno and Arakawa, 2004). All these results reinforce the confidence in the relevance of the DEM
497 model.

498 We acknowledge that the mechanical parameters obtained from minimising the logarithmic relative errors on the statistical
499 indicators do not necessarily represent optimal values, in the sense that only a limited number of parameter sets could be tested.
500 Based on the sensitivity analysis, a more proper inversion procedure could be developed to retrieve true optimal values of the
501 mechanical parameters. This would certainly provide more robust elements as to whether a single set of mechanical parameters
502 can be used to represent the experimental results of all snow types, or whether these mechanical parameters differ according

503 to the snow type. Our current analysis cannot provide a conclusive answer to this question. Note that ice is a polycrystalline
504 material, whose mechanical behaviour can be strongly anisotropic depending on the ice structure (Fish and Zaretsky 1997;
505 Thorsteisson, 2001; e.g. Maeno and Arakawa, 2004). Therefore, it is not unlikely that ice bonds between grains could be
506 characterised by different mechanical properties depending on the specific conditions of snow formation and evolution.
507 As further proof of DEM predictive capabilities, we could also observe that the grain displacement fields measured for the
508 different snow types were overall well reproduced by the simulations (Figs. 7 and 8). In particular, the model captures the
509 radial extent of the deformation zone, which is on the order of $1.5R$ - $2.2R$. A discrepancy between the numerical and
510 experimental radial displacement profiles was observed for the RGlR sample. However, it can be noted that these experimental
511 radial displacement profiles for the RGlR sample also show the largest divergence with the prediction of the cavity expansion
512 model (CEM) (Yu and Carter, 2002), as shown by Peinke et al. (2020). In fact, the radial profile predicted by the CEM for this
513 sample is similar to the radial profile obtained numerically in this study.

514 **4.2 Interpretation**

515 **4.2.1 Sensitivity to the mechanical parameters**

516 The sensitivity analysis revealed a strong influence of the mechanical parameters on the simulation results. In particular, a
517 clear dependence of the mean macroscopic force with Young's modulus E was observed, suggesting that a significant part of
518 the sample undergoes elastic deformation, while brittle failures are confined in a region close to the tip. Note that a similar
519 dependence to E with a cohesive contact law has been observed in DEM modelling of soil compression (De Pue et al., 2019)
520 and snow compression (Bobillier et al., 2020). The mean macroscopic force, the amplitude of force fluctuations and the
521 correlation length all increase with the cohesion C and, to a smaller extent, with the friction coefficient $\tan(\phi)$. This can be
522 related to the fact that increasing cohesion and friction between grains increase bond strength. It was also observed that
523 cohesion tends to prevent bond failures and to favour the upward movement of grains for samples with a large initial density,
524 such as RGlR. In contrast, increasing the friction coefficient enhances the bond failure rate and the downward movement of
525 grains (Figs. S12, S16, S20, S24). When sliding between grains is inhibited, a grain dragged by the tip movement will entrain
526 surrounding grains more easily, thus enlarging the deformation zone and triggering additional bond failures. Finally, radial
527 grain displacements and the radius of the deformation zone appeared to be mostly insensitive to the mechanical parameters,
528 indicating that these features are mainly controlled by CPT configuration and snow microstructure.

529 **4.2.2 Compaction zone development**

530 For all snow types, the force profiles computed numerically display a 'S' shape (Figs. 1, S6, S8, S10). We attribute this shape
531 to the development of a compaction zone (CZ) in front of the tip during its penetration into the numerical sample. More
532 specifically, the first stage of the force profiles (slope increase) is presumably caused by the progressive entry of the cone into
533 the sample. The second stage (constant slope) is attributed to the development of the CZ in front of the tip. The third stage

534 (quasi-constant force value) suggests that a steady-state regime, with a fully-developed CZ, is reached. Depending on the snow
535 type, the numerical results indicate that full development of the CZ occurs for 6 mm to 8 mm of penetration depth. These
536 results agree with the experimental profiles for the RG, DH and PP samples. Globally, we can highlight that the DEM
537 simulations are able to reproduce fairly well the global shape of the experimental profiles, and thus to correctly capture the
538 development of the CZ.

539 Nevertheless, in another experimental study, the CZ has been reported to be fully developed only for around 40 mm of depth
540 penetration (Herwijnen, 2013), which is significantly deeper than the experimental and numerical results obtained in this study.
541 A first hypothesis to explain this discrepancy is that since the maximum depth of our CPT force profiles is 10 mm, we might
542 miss information on the full CZ development. A second explanation could be related to the differences in the experimental
543 setups. Indeed, Peinke et al. (2020) performed CPT on snow samples contained in cylinders of 20 mm diameter and 20 mm
544 height, which is significantly smaller than the decimetric snow samples considered by Herwijnen (2013). Boundary effects
545 might thus play a role in limiting the development of the CZ. Finally, the tip geometry also differs between the two studies.
546 Peinke et al. (2020) used a plain tip, while Herwijnen (2013) used the original SMP tip geometry with a cone radius larger
547 than the rod. A sensitivity analysis comparing the two geometries showed an influence over the upper 12 mm of the force
548 profiles (Peinke, 2020). The plain tip geometry resulted in larger values of the mean macroscopic force and the amplitude of
549 force fluctuations values. This effect might also influence the characteristics of the CZ development, which could be studied
550 in the future using the presented numerical model.

551 **4.2.3 Grain-tip interaction**

552 The sensitivity analysis to the grain shape representation (Sect. S1.1) provides interesting insights into the interpretation of
553 force profiles. In particular, the study highlighted that the grain shape representation could be relatively coarse (high volumetric
554 error E_V) but still produce a force profile with an acceptable mechanical error E_M compared to a reference profile obtained for
555 a fine grain shape representation ($E_V < 10\%$) (Fig. S1, Table S1). This is notably the case for the RG sample, for which the
556 selected grain shape representation ($L = 5, S = 0.3$) corresponds to a value of E_V of about 40%. Large values of E_V often imply
557 grain loss, as the smallest grains identified in the μ CT scans cannot be represented by the DEM with coarse spherical elements.
558 Yet, the similarity of the force profile to the reference force profile indicates the limited contribution of these smallest grains
559 to the macroscopic force, compared to the largest grains with stronger bonds. The loss of grains and bonds might nevertheless
560 directly affect the force fluctuations, providing a potential explanation as to why the DEM model underestimates the correlation
561 length obtained experimentally for the samples with the smallest grain sizes (RG and PP) (Figs. 5, S23).

562 **4.2.3 Scaling relation for the mean macroscopic force**

563 To try and synthesise the large number of simulation results obtained in this study, scaling relations describing the evolution
564 of the statistical indicators as a function of the main simulation parameters can be looked for. We focused in particular on the
565 mean macroscopic force \bar{F} , which was observed to depend both on the mechanical parameters E , C and $\tan(\varphi)$, as well as on

566 sample microstructure. Since the range of friction coefficient values (between 0.2-0.5) that we could explore remained limited
 567 compared to the ranges of E and C , the parameter $\tan(\varphi)$ was not included in this analysis and the results presented below
 568 correspond to a single value $\tan(\varphi) = 0.3$.

569 First, inspection of our results (see Figs. 5 (a), S15 (a), S19 (a), S23 (a)) indicates that the dependencies of the mean
 570 macroscopic force \bar{F} to the Young's modulus E and cohesion C appear to be consistent across the four tested samples (see also
 571 Table S4). More precisely, \bar{F} scales with E according to a power law of the form $\bar{F} \sim E^{-\alpha}$, with an exponent α on the order of
 572 $1/2$. Similarly, \bar{F} scales with C according to a power law of the form $\bar{F} \sim C^\beta$, with β on the order of $3/2$.

573 Second, we can expect \bar{F} to be also related to the rate of cohesive broken bonds per unit penetration depth. In particular, it is
 574 observed (see Figs. S12, S16, S20, S24) that the slope λ of the cumulative proportion of broken bonds as a function of depth
 575 is essentially independent of the Young's modulus and cohesion. Conversely, as shown in Fig. 9 (a), this slope λ is linearly
 576 related to the initial contact density ν defined as:

$$577 \nu = z\Phi \tag{10}$$

578 with z the coordination number (number of initial cohesive interactions between grains divided by the number of grains, see
 579 Table 1) and Φ the volume fraction of the sample (ice density = 917 kg m^{-3} , see Table 1).

580

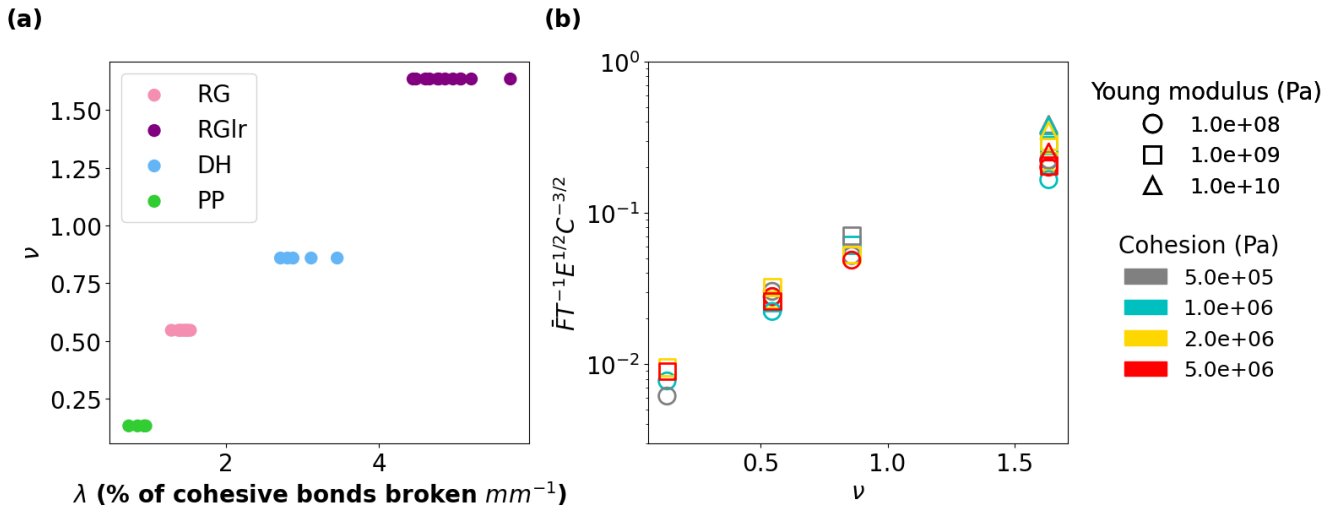
581 From these different observations, the following scaling law for the mean macroscopic force \bar{F} can be proposed:

$$582 \bar{F} = B T C \left(\frac{C}{E}\right)^\alpha f(\nu) \tag{11}$$

583 with B a dimensionless constant, T (m^2) the surface area of the cone (with a radius R and a cone apex a , Table 2) in contact
 584 with the sample, and f a function to be determined. Figure 9 (b) shows the dimensionless quantity $\bar{F}T^{-1}E^{1/2}C^{-3/2}$ plotted against
 585 the initial contact density ν . We observe that all the simulation results for the four snow types and the different values of
 586 Young's modulus and cohesion nicely merge on a unique logarithmic trend. Note, however, that a relatively larger dispersion
 587 is observed for RGIr ($\nu = 1.63$) compared to the other samples.

588 Equation (11) encapsulates in a single relation the main physics controlling the mean macroscopic force recorded by the
 589 penetrometer. In particular, this relation indicates that the influence of snow microstructure can be captured, at least as a first
 590 approximation, by the initial contact density ν . Former studies already showed that this parameter plays a key role in the
 591 mechanical behaviour of cohesive granular materials (Gaume et al. 2017). Looking for similar relations describing the other
 592 statistical indicators (amplitude of force fluctuations and correlation length) constitutes an interesting prospect for future
 593 analyses, although we can anticipate these indicators to display more complex dependencies. Further analyses will also be
 594 required to explore the influence of the friction coefficient on these relations.

595



596

597 **Figure 9: (a) Initial contact density ν versus the slope λ of the proportion of cohesive bonds broken per unit depth (mm^{-1}) for each**
 598 **snow type. The values of initial contact density ν were computed with Eq. (10) and the values indicated in Table 1. The slopes λ were**
 599 **computed from the evolution of the cumulative proportion of cohesive bonds broken (Figs. S12, S16, S20, S24) over a window of 7**
 600 **mm depth. (b) Dimensionless quantity $\bar{F}T^{-1}E^{1/2}C^{-3/2}$ (see Eq. (11)) versus the initial contact density ν for all simulation results. All the**
 601 **results are provided for a friction coefficient $\tan(\phi)$ of 0.3.**

602

603 5 Conclusion

604 We have evaluated a numerical model based on DEM that reproduces the mechanical behaviour of snow in the brittle regime.
 605 The DEM model takes into account the ice properties and the snow microstructure captured by tomography. The experimental
 606 configuration of the CPT measurements conducted on different snow types by Peinke et al. (2020) has been reproduced with
 607 the DEM model. Three parameters namely, the mean macroscopic force, the amplitude of force fluctuations and the correlation
 608 length, were used to quantify the similitude of the numerical and experimental profiles. The grains displacement field was
 609 computed and compared to the experimental displacement field derived from μ CT scans acquired before and after the CPT.
 610 The DEM model has demonstrated overall a good capability to reproduce the mechanical responses of CPT performed in
 611 different snow types. The computed force profiles satisfactorily reproduce the main characteristics of the experimental force
 612 profiles. The results revealed that the force profile characteristics are strongly dependent on the microstructure. A sensitivity
 613 analysis also demonstrated the dependence of the mechanical response to the mechanical parameters of the contact law. In
 614 particular, a simple scaling law could be derived relating the mean macroscopic force computed by the DEM to the mechanical
 615 parameters E (Young's modulus) and C (cohesion) and to the microstructure characteristics captured by the initial contact
 616 density. The displacement fields are also well reproduced by the model, except for the RGlR sample showing a larger extent
 617 for the numerical results. The agreement in terms of radial displacement profiles is very good. The grains are mainly travelling

618 downward during the CPT, although for the RGIr sample, the upward movements close to the surface are not negligible. The
619 CPT implies a complex deformation field with a compression zone around the apex and an expansion zone close to the surface
620 (Peinke et al., 2020). Therefore being able to reproduce the force profiles (including high-frequency fluctuations) and
621 displacement fields for this mechanical test constitutes a strong validation of the reliability of the DEM model.
622 However, a downside of the DEM method is its high computational cost (simulation times ranging between 1 week to several
623 months depending on the physical and numerical parameters for the chosen CPT configuration), which limited the range of
624 mechanical parameters that could be explored for all snow types. The developed DEM model nonetheless constitutes a versatile
625 approach that could be applied to various materials and configurations in future studies. In particular, it will be possible to use
626 the model to gain more physical insights into the interaction between the tip and the grains, in order to better interpret the CPT
627 force profiles. Such analyses will provide ways to test and derive relevant macro- and micromechanical parameters to
628 characterise the microstructure properties from the CPT force signal solely. In particular, the validity of the assumptions made
629 by the HPP-NHPP method, as well as the influence of the CZ development, will be assessed. Future studies may also consider
630 refining the used contact laws to investigate, e.g. the influence of sintering processes on CPT results.

631 **Code availability**

632 Codes can be provided by the corresponding author upon request.

633 **Data availability**

634 All data can be provided by the corresponding author upon request.

635 **Author contribution**

636 CH, PH and GC developed the numerical model, CH performed simulations and evaluated the numerical model, IP, PH, GC,
637 JR designed experiment, IP acquired experimental data, IP processed and analysed experimentation measurements, CH
638 analysed and interpreted numerical results, CH wrote the manuscript draft, PH and GC reviewed and edited the manuscript.

639 **Competing interests**

640 GC is a member of the editorial board of The Cryosphere. The peer-review process was guided by an independent editor, and
641 the authors have no other competing interests to declare.

642 **Acknowledgements**

643 This work benefited from financial supports from the Centre National de la Recherche Scientifique (CNRS), the Centre
644 National de la Recherche Météorologique, the Agence Nationale de la Recherche (Project ANR MiMESis-3D ANR-19-CE01-
645 0009). We thank the two reviewers, Richard Parson and Henning Löwe, for their constructive feedback that enabled us to
646 significantly improve the quality of our manuscript.

647 **References**

- 648 Bartelt, P., and M. Lehning.: A physical SNOWPACK model for the Swiss avalanche warning: Part I—Numerical model,
649 Cold Reg. Sci.Technol.,35(3), 123–145, doi: 10.1016/S0165-232X(02)00074-5, 2002.
- 650 Bishop, R. F., Hill, R., and F Mott, N.: The theory of indentation hardness tests, Proc. Phys. Soc. 57:321, doi: 10.1088/0959-
651 5309/57/3/301, 1945.
- 652 Bobillier, G., Bergfeld, B., Capelli, A., Dual, J., Gaume, J., Herwijnen, A., and Schweizer, J.: Micromechanical modeling of
653 snow failure, The Cryosphere, 14, 39–49, doi:10.5194/tc-14-39-2020, 2020.
- 654 Bobillier, G., Bergfeld, B., Dual, J., Gaume, J., Herwijnen, A., and Schweizer, J.: Micro-mechanical insights into the dynamics
655 of crack propagation in snow fracture experiments, Sci Rep 11, 11711, doi :10.1038/s41598-021-90910-3, 2021.
- 656 Bolton, M. D., Gui, M. W., and Phillips, R.: “Review of miniature soil probes for model tests,” in Proceedings of the 11th
657 Southeast Asian Geotechnical Conference (Singapore), 85–90, 1993.
- 658 Brun, E., David, P., Sudul, M., and Brunot, G.: A numerical model to simulate snow-cover stratigraphy for operational
659 avalanche forecasting, J. Glaciol., 38(128), 13–22, doi: 10.3189/S0022143000009552, 1992.
- 660 Calonne, N., F. Flin, C. Geindreau, B. Lesaffre and S. Rolland du Roscoat: Study of a temperature gradient metamorphism of
661 snow from 3-D images: time evolution of microstructures, physical properties and their associated anisotropy, The Cryosphere,
662 8, 2255-2274, doi: 10.5194/tc-8-2255-2014, 2014.
- 663 Calonne, N., F. Flin, B. Lesaffre, A. Dufour, J. Roulle, P. Puglièse, A. Philip, F. Lahoucine, C. Geindreau, J.-M. Panel, S.
664 Rolland du Roscoat and P. Charrier, CellDyM : a room temperature operating cryogenic cell for the dynamic monitoring of
665 snow metamorphism by time-lapse X-ray microtomography, Geophys. Res. Lett., 42, doi: 10.1002/2015GL06354, 2015.
- 666 Coléou, C., B. Lesaffre, J.-B. Brzoska, W. Ludwig and E. Boller: Three dimensional snow images by X-ray microtomography,
667 Ann. Glaciol., 32, 75-81, doi : 10.3189/172756401781819418, 2001.

668 Coeurjolly, D., Montanvert, A. and Chassery, J.-M.: Descripteurs de forme et moments géométriques. *Géométrie discrète et*
669 *images numériques*, Hermès, 2007.

670 De Pue, J., Di Emidio, G., Verastegui Flores, R. D., Bezuijen, A., and Cornelis, W. M.: Calibration of DEM material parameters
671 to stimulate stress-strain behaviour of unsaturated soils during uniaxial compression, *Soil and Tillage Research*, 194, 104303,
672 doi: 10.1016/j.still.2019.104303, 2019.

673 Dowd, T. and Brown, R.L.: A new instrument for determining strength profiles in snow cover, *Journal of Glaciology*, 32(111):
674 299–301, doi: 10.3189/S0022143000015628, 1986.

675 Fierz, C., Armstrong, R. L., Durand, Y., Etchevers, P., Greene, E., and McClung, D. M.: “The international classification for
676 seasonal snow on the ground,” in *Tech. Doc. Hydrol. 83 Paris: UNESCO*, 2009.

677 Fish, A. M. and Zaretsky, Y. K.: Ice strength as a function of hydrostatic pressure and temperature, CRREL report, 38207814,
678 1997.

679 Floyer, J.A., and Jamieson, J.B. Rate-effect experiments on round-tipped penetrometer insertion into uniform snow, *Journal*
680 *of Glaciology*, 56(198): 664–672. doi:10.3189/002214310793146322, 2010.

681 Freitag, J., Wilhelms, F. and Kipfstuhl, S.: Microstructure dependent densification of polar firn derived from X-ray
682 microtomography, *J. Glaciol.*, 50(169), 243–250, doi: 10.3189/172756504781830123, 2004.

683 Gammon, P. H., Kieft; H., Clouter, M. J. and Denner, W. W.: Elastic constants of artificial and natural ice samples by Brillouin
684 spectroscopy, *Journal of Glaciology*, 29(103), 433–460, doi: 10.3189/S0022143000030355, 1983.

685 Gaume, J., van Herwijnen, A., Chambon, G., Birkeland, K. W., and Schweizer, J.: Modeling of crack propagation in weak
686 snowpack layers using the discrete element method, *The Cryosphere*, 9, 1915–1932. doi: 10.5194/tc-9-1915-2015, 2015.

687 Gaume, J., van Herwijnen, A., Chambon, G., Wever, N., and Schweizer, J.: Snow fracture in relation to slab avalanche release:
688 Critical state for the onset of crack propagation, *The Cryosphere*, 11(1), 217–228, doi: 10.5194/tc-11-217-2017, 2017.

689 Gaume, J., Löwe, H., Tan, S., and Tsang, L.: Sacaling laws for the mechanics of loose and cohesive granular materials based
690 on Baxter’s sticky hard spheres, *Physical Review E*, 96, 032914, doi: 10.1103/PhysRevE.96.032914, 2017.

691 Gubler, H. U.: On the ramsonde hardness equation, *IAHS-AISH Publ.* 114, 110–121, 1975.

692 Gubler, H. U.: Determination of the mean number of bonds per snow grain and of the dependence of the tensile strength of
693 snow on stereological parameters, *J. Glaciol.* 20, 329–341, doi: 10.3189/S0022143000013885, 1978.

694 Hagenmuller, P., Chambon, G., Lesaffre, B., Flin, F., and Naaim, M.: Energy-based binary segmentation of snow
695 microtomographic images, *J. Glaciol.* 59 (217), 859–873, doi: 10.3189/2013JoG13J035, 2013.

696 Hagenmuller, P., Calonne, N., Chambon, G., Flin, F., Geindreau, C., and Naaim, M.: Characterization of the snow
697 microstructural bonding system through the minimum cut density, *Cold Reg. Sci. Technol.* 108, 72–79, doi:
698 10.1016/j.coldregions.2014.09.002, 2014.

699 Hagenmuller, P., Chambon, G., Flin, F., Morin, S., and Naaim, M.: Snow as a granular material: assessment of a new grain
700 segmentation algorithm, *Gran. Matter* 16 (4), 421–432, doi: 10.1007/s10035-014-0503-7, 2014.

701 Hagenmuller, P., Chambon, G., and Naaim, M.: Microstructure-based modeling of snow mechanics: A discrete element
702 approach, *Cryosphere*, 9(5), 1969–1982, doi: 10.5194/tc-9-1969-2015, 2015.

703

704 Heggli, M., B. Köchle, M. Matzl, B. R. Pinzer, F. Riche, S. Steiner, D. Steinfeld, and M. Schneebeli: Measuring snow in 3-D
705 using X-ray tomography: Assessment of visualization techniques, *Ann. Glaciol.*, 52(58), 231–236,
706 doi:10.3189/172756411797252202, 2011.

707 Herwijnen, A. V.: Experimental analysis of snow micropenetrometer (SMP) cone penetration in homogeneous snow layers,
708 *Can. Geotech. J.* 50, 1044–1054. doi: 10.1139/cgj-2012-0336, 2013.

709 Jamieson, J. B., and Johnston, C. D.: Snowpack characteristics associated with avalanche accidents, *Canadian Geotechnical*
710 *Journal*, 29(5), 862–866, doi: 10.1139/t92-093, 1992.

711 Johnson, J., and Schneebeli, M.: Characterizing the microstructural and microchemical properties of snow, *Cold Reg. Sci.*
712 *Technol.* 30, 91–100. doi: 10.1016/S0165232X(99)00013-0, 1999.

713 Johnson, J. B. and Hopkins, M. A.: Identifying microstructural deformation mechanisms in snow using discrete-element
714 modeling, *J. Glaciol.*, 51, 432–442. doi: 10.3189/172756505781829188, 2005.

715 Kozak, M. C., Elder, K., Birkeland, K., and Chapman, P.: Variability of snow layer hardness by aspect and prediction using
716 meteorological factors, *Cold Regions Science and Technology*, 37(3): 357–371. doi:10.1016/S0165-232X(03)00076-4, 2003.

717 Lunne, T., Robertson, P. K., and Powell, J. J. M.: *Cone penetration testing in geotechnical practice*. Blackie Academic, EF
718 Spon/Routledge, New York, 1997.

719 LeBaron, A., Miller, D., and van Herwijnen, A.: Measurements of the deformation zone around a split-axis snow
720 micropenetrometer tip, *Cold Reg. Sci. Technol.* 97, 90–96. doi: 10.1016/j.coldregions.2013.10.008, 2014.

721 Lowe, H., and van Herwijnen, A.: A Poisson shot noise model for micropenetration of snow, *Cold Regions Science and*
722 *Technology*, 70: 62–70. doi: 10.1016/j.coldregions.2011.09.001, 2012.

723 McCallum, A.: A brief introduction to cone penetration testing (CPT) in frozen geomaterials, *Ann. Glaciol.* 55, 7–14. doi:
724 10.3189/2014 AoG68A005, 2014.

725 Mackenzie, R., and Payten, W.: A portable, variable-speed, penetrometer for snow pit evaluation, In *Proceedings of the 2002*
726 *International Snow Science Workshop*, Penticton, B.C. pp. 294–300, 2002.

727 Maeno, N. and Arakawa, M.: Adhesion shear theory of ice friction at low sliding velocities, combined with ice sintering,
728 *Journal of Applied Physics*, 95(1), 134–139, doi: 10.1063/1.1633654, 2004.

729 Marshall, H.P., and Johnson, J.B.: Accurate inversion of high-resolution snow penetrometer signals for microstructural and
730 micromechanical properties, *Journal of Geophysical Research: Earth Surface*, 114(F4): F04016. doi: 10.1029/2009JF001269,
731 2009.

732 Mede, T., Chambon, G., Hagenmuller, P., and Nicot, F.: A medial axis based method for irregular grain shape representation
733 in DEM simulations, *Granular Matter*, 20(1), 1–11, doi: 10.1007/s10035-017-0785-7, 2018a.

734 Mede, T., Chambon, G., Hagenmuller, P., and Nicot, F.: Snow failure modes under mixed loading, *Geophys. Res. Lett.* 45
735 (24), 13–351, doi: 10.1029/2018GL080637, 2018b.

736 Mede, T., Chambon, G., Nicot, F., and Hagenmuller, P.: Micromechanical investigation of snow failure under mixed-mode
737 loading, *International Journal of Solids and Structures*, 199, 95–108. doi:10.1016/j.ijsolstr.2020.04.020, 2020.

738 Montagnat, M., Löwe, H., Calonne, N., Schneebeli, M., Matzl, M. and Jaggi, M.: On the birth of structural and crystallographic
739 fabric signals in polar snow: A case study from the EastGRIP snowpack, *Frontiers in Earth Science*, 8:365.
740 doi:10.3389/feart.2020.00365, 2020.

741 Narita, H.: An experimental study on tensile fracture of snow, *Contribut. Inst. Low Temperat. Sci.* A32, 1–37, 1983.

742 Peinke, I., Hagenmuller, P., Chambon, G., and Roulle, J.: Investigation of snow sintering at microstructural scale from micro-
743 penetration tests, *Cold Reg. Sci. Technol.* 162, 43–55. doi: 10.1016/j.coldregions.2019.03.018, 2019.

744 Peinke, I., Hagenmuller, P., Andò, E., Chambon, G., Flin, F. and Roulle, J.: Experimental Study of Cone Penetration in Snow
745 Using X-Ray Tomography, *Front. Earth Sci.* 8:63. doi: 10.3389/feart.2020.00063, 2020.

746 Proksch, M., Löwe, H., and Schneebeli, M.: Density, specific surface area, and correlation length of snow measured by high-
747 resolution penetrometry, *J. Geophys. Res. Earth Surf.* 120, 346–362. doi: 10.1002/2014JF003266, 2015.

748 Reuter, B., Schweizer, J., and van Herwijnen, A.: A process-based approach to estimate point snow instability, *Cryosphere*, 9,
749 837–847. doi: 10.5194/tc-9-837-2015, 2015.

750 Reuter, B., Proksch, M., Löwe, H., Van Herwijnen, A., and Schweizer, J.: Comparing measurements of snow mechanical
751 properties relevant for slab avalanche release, *J. Glaciol.* 65, 55–67. doi: 10.1017/jog.2018.93, 2019.

752 Ruiz, S., Straub, I., Schymanski, S. J., and Or, D.: Experimental evaluation of earthworm and plant root soil penetration-cavity
753 expansion models using cone penetrometer analogs, *Vadose Zone J.* 15, 1–14. doi: 10.2136/vzj2015.09.0126, 2016.

754 Ruiz, S., Capelli, A., van Herwijnen, A., Schneebeli, M., and Or, D.: Continuum cavity expansion and discrete
755 micromechanical models for inferring macroscopic snow mechanical properties from cone penetration data, *Geophys. Res.*
756 *Lett.* 44, 8377–8386. doi: 10.1002/2017GL074063, 2017.

757 Shapiro, L.H., Johnson, J. B., Sturm, M., and Blaisdell, G. L.: Snow mechanics: review of the state of knowledge and
758 applications, *CRREL Rep.* 97-3, 1997.

759 Schaap, L. H. J. and Fohn, P. M. B.: Cone penetration testing in snow, *Canadian Geotechnical Journal* 24(3):335-341.
760 doi:10.1139/t87-044, 2011.

761 Schneebeli, M.: Numerical simulation of elastic stress in the microstructure of snow, *Annals of Glaciology*, 38. doi:
762 10.3189/172756404781815284, 2004.

763 Schneebeli, M., and Johnson, J. B.: A constant-speed penetrometer for high resolution snow stratigraphy, *Annals of*
764 *Glaciology*, 26: 107–111, doi: 10.3189/1998AoG26-1-107-111, 1998.

765 Schneebeli, M., and Sokratov, S. A.: Tomography of temperature gradient metamorphism of snow and associated changes in
766 heat conductivity, *Hydrol. Process.*, 18(18), 3655–3665, doi: 10.1002/hyp.5800, 2004.

767 Schulson, E. M. and Duval, P.: *Creep and Fracture of Ice*, Cambridge University Press, 2009.

768 Schweizer, J., Jamieson, J. B., and Schneebeli, M.: Snow avalanche formation, *Rev. Geophys.*, 41(4), 1016.
769 doi:10.1029/2002RG000123, 2003.

770 Šmilauer, V., Catalano, E., Chareyre, B., Dorofeenko, S., Duriez, J., Gladky, A., Kozicki, J., Modenese, C., Scholtès, L.,
771 Sibille, L., Stransky, J., and Thoeni, K.: Yade reference documentation. In V. Šmilauer (Ed.), *Yade Documentation* (Vol. 474).
772 Retrieved from <http://yadedem.org/doc>, 2010/

773 Thorsteinsson, T.: An analytical approach to deformation of anisotropic ice-crystal aggregates, *Journal of Glaciology*, 47
774 (158), 507-516, doi: 10.3189/172756501781832124, 2001.

775 Vionnet, V., Brun, E., Morin, S., Boone, A., Faroux, S., Le Moigne, P., Martin, E. and Willemet, J.-M.: The detailed snowpack
776 scheme Crocus and its implementation in SURFEX v7.2, *Geosci. Model Dev.*, 5, 773-791. doi: 10.5194/gmd-5-773-2012,
777 2012.

778 Wautier, A., Geindreau, C., and Flin, F.: Linking snow microstructure to its macroscopic elastic stiffness tensor: A numerical
779 homogenization method and its application to 3-D images from x-ray tomography, *Geophysical Research Letters*, 42, 8031–
780 8041. <https://doi.org/10.1002/2015GL065227>, 2015.

781 Yu, H. S., and Carter, J.: Rigorous similarity solutions for cavity expansion in cohesive-frictional soils, *Int. J. Geomech.*, 2,
782 233–258. doi:10.1061/(ASCE)1532-3641(2002)2:2(233), 2002.